



| | |
|----------------------------------|---|
| Publication Year | 2017 |
| Acceptance in OA | 2020-08-20T10:00:59Z |
| Title | The NGC 454 system: anatomy of a mixed ongoing merger |
| Authors | Plana, H., RAMPAZZO, Roberto, MAZZEI, Paola, Marino, A., Amram, Ph., Ribeiro, A. L. B. |
| Publisher's version (DOI) | 10.1093/mnras/stx2091 |
| Handle | http://hdl.handle.net/20.500.12386/26737 |
| Journal | MONTHLY NOTICES OF THE ROYAL ASTRONOMICAL SOCIETY |
| Volume | 472 |



The NGC 454 system: anatomy of a mixed ongoing merger

H. Plana,^{1★} R. Rampazzo,^{2★} P. Mazzei,² A. Marino,² Ph. Amram³
and A. L. B. Ribeiro¹

¹Laboratório de Astrofísica Teórica e Observacional, Universidade Estadual de Santa Cruz, 45650-000 Ilhéus-BA, Brazil

²INAF–Osservatorio Astronomico di Padova, Vicolo dell’Osservatorio 5, I-35122 Padova, Italy

³Aix Marseille Univ., CNRS, Laboratoire d’Astrophysique de Marseille (LAM), 38 rue Frédéric Joliot-Curie, F-13388 Marseille Cedex 13, France

Accepted 2017 August 10. Received 2017 August 9; in original form 2017 May 16

ABSTRACT

This paper focuses on NGC 454, a nearby interacting pair of galaxies (AM 0112-554, RR23), composed of an early-type (NGC 454 E) and a star-forming late-type companion (NGC 454 W). We aim at characterizing this wet merger candidate via a multi- λ analysis, from near-UV (NUV) to optical using *Swift* UV/Optical Telescope (UVOT), and mapping the $H\alpha$ intensity (I) distribution, velocity (V_r) and velocity dispersion (σ) fields with SAM+Fabry–Perot@SOAR observations. Luminosity profiles suggest that NGC 454 E is an S0. Distortions in its outskirts caused by the ongoing interaction are visible in both optical and NUV frames. In NGC 454 W, the NUV-UVOT images and the $H\alpha$ show a set of star-forming complexes connected by a faint tail. $H\alpha$ emission is detected along the line connecting NGC 454 E to the NGC 454 main $H\text{II}$ complex. We investigate the $(I-\sigma)$, $(I-V_r)$ and $(V_r-\sigma)$ diagnostic diagrams of the $H\text{II}$ complexes, most of which can be interpreted in a framework of expanding bubbles. In the main $H\text{II}$ complex, enclosed in the UV brightest region, the gas velocity dispersion is highly supersonic reaching 60 km s^{-1} . However, $H\alpha$ emission profiles are mostly asymmetric indicating the presence of multiple components with an irregular kinematics. Observations point towards an advanced stage of the encounter. Our smoothed particle hydrodynamic simulations with chemo-photometric implementation suggest that this mixed pair can be understood in terms of a 1:1 gas/halo encounter giving rise to a merger in about 0.2 Gyr from the present stage.

Key words: galaxies: elliptical and lenticular, cD – galaxies: interactions – galaxies: irregular – galaxies: kinematics and dynamics – galaxies: photometry.

1 INTRODUCTION

Interactions modify the gravitational potential of the involved galaxies and may lead to their merger. During the interaction, the stellar and gas components of each galaxy respond differently to the potential variation. The outcome is directly measurable in terms of morphology, kinematics and, in general, of the physical properties of each galaxy, such as their star formation rate and AGN activity. A comprehensive description of the *job of interactions* in shaping galaxies and their properties as investigated in last decades of extragalactic research is widely presented and discussed by Struck (2011, and references therein).

Pairs of galaxies have been used as probes to study interactions. Well-selected samples of pairs and catalogues have been produced (see e.g. Karachentsev 1972; Peterson 1979; Rampazzo et al. 1995; Soares et al. 1995; Barton 2000). Single studies as well as surveys of pair catalogues have been crucial to reveal several interaction

effects once compared to isolated/unperturbed galaxy samples (see e.g. Rampazzo et al. 2016, section 5.3.2).

Although the vast majority of pair members have similar morphological types, a first light on the existence of mixed morphology pairs has been shed by the Karachentsev (1972) Catalog of Isolated Pairs. Rampazzo & Sulentic (1992) estimated that between as much as 10 and 25 per cent of the pairs in any complete (non-hierarchical) sample will be of the mixed morphology type. At the beginning of 1990s, studies about this kind of pairs were addressed to ascertain possible enhancement of the star formation activity, with respect to non-interacting samples, via mid- and far-infrared (FIR) observations, at that time often hampered by a low resolution (see e.g. Xu & Sulentic 1991; Surace et al. 1993). Mixed morphology pairs have been thought as the cleanest systems where to verify possible mass transfer between the gas-rich and the gas-poor member, typically the early-type companion. Several candidates of mixed morphology pairs with star formation and AGN activity, fuelled by gas transfer between components, have been indicated (see e.g. de Mello, Sulentic & Rampazzo 1995; Rampazzo et al. 1995; de Mello et al. 1996; Domingue et al. 2003). The literature reports

* E-mail: plana@uesc.br (HP); roberto.rampazzo@oapd.inaf.it (RR)

in general a star formation enhancement in wet and mixed pairs (see e.g. Larson & Tinsley 1978; Combes et al. 1994; Barton 2000; Barton Gillespie, Geller & Kenyon 2003; Smith et al. 2007, 2016; Knapen & Querejeta 2015).

The fate of mixed, gravitationally bound pairs is to merge; the available gas may trigger star formation for some time, but it is still unclear what will be the merger product. The role of mixed merger has been investigated by Lin et al. (2008) who suggested that roughly 36 per cent of the present-day red galaxies, typically early-type galaxies, have experienced a mixed merger. According to these authors, mixed (and wet) mergers will produce red galaxies of intermediate mass, after the quenching of the star formation, while the more massive part of the red sequence should be generated by stellar mass growth via dry mergers (van Dokkum 2005; Faber et al. 2007).

In the context of star formation, the dynamics of the (ionized, neutral and molecular) gas clouds during interaction is a crucial topic. H I bridges as well as clouds larger than $10^8 M_{\odot}$ are detected in wet interacting/merging pairs with $20\text{--}40 \text{ km s}^{-1}$ velocity dispersion (see e.g. Elmegreen, Kaufman & Thomasson 1993; Irwin 1994; Elmegreen et al. 1995). External gas high velocity dispersion is possibly linked to an internal high velocity dispersion of the clouds, increasing the star formation efficiency. Combes et al. (1994) suggest that the enhancement of the star formation in wet interacting galaxies may be connected to an increase of the molecular gas that inflows towards the centre by tidal torque. There are indications that the brightness distribution of H II regions in interacting objects differs from unperturbed ones. Bright H II regions can form by gas flows during interaction. They are on average brighter than in isolated galaxies and have a high internal velocity dispersion ($15\text{--}20 \text{ km s}^{-1}$) as reported by Zaragoza-Cardiel et al. (2015). Furthermore, the number of H II regions in interacting objects is larger than in isolated galaxies with the same absolute magnitude, suggesting that interactions do in fact increase the star formation rate.

The subject of the present study is the NGC 454 system, a strongly peculiar, interacting (AM 0112-554; Arp & Madore 1987) and isolated Reduzzi & Rampazzo (1995, RR23) pair in the Southern hemisphere. Johansson (1988) described the system as ‘a pair of emission-line galaxies in close interaction, or in the early stage of a merger, consisting of a large elliptical and a blue irregular galaxy’. Fig. 1 dissects the system according to the regions labelled by Johansson (1988) and Stiavelli et al. (1998). We will adopt their definition along this paper adding the prefix NGC 454.

The East part of the system (labelled E in Fig. 1, NGC 454 E hereafter) identifies the early-type member of the pair. NGC 454 E is crossed by dust lanes and it is distorted by the interaction. The *U*, *B*, *V* Johnson and Gunn *I* photometry by Johansson (1988) presented the East member as a red elliptical with a luminosity profile that follows closely an $r^{1/4}$ law (de Vaucouleurs 1948) out to 15 arcsec from the galaxy centre. The Stiavelli et al. (1998) high-resolution *Hubble Space Telescope* (*HST*) imaging, in the *F450W*, *F606W* and *F814W* filters, shows that NGC 454 E is likely an S0. Their luminosity profile, extending out to ≈ 30 arcsec, is much better fitted by two components: an $r^{1/4}$ law describing the bulge plus an exponential law (Freeman 1970) for a disc. The $(B - V)$ colour profile indicates that the central part of the galaxy, i.e. $r \leq 1$ arcsec, is red with $1 \lesssim (B - V) \lesssim 1.4$ while the outside region is slightly bluer with $0.8 \lesssim (B - V) \lesssim 1$. The nucleus of NGC 454 E, observed spectroscopically by Johansson (1988), revealed several emission lines and matched two of the empirical criteria proposed by Shuder & Osterbrock (1981) for a Seyfert galaxy: the line width of H α is

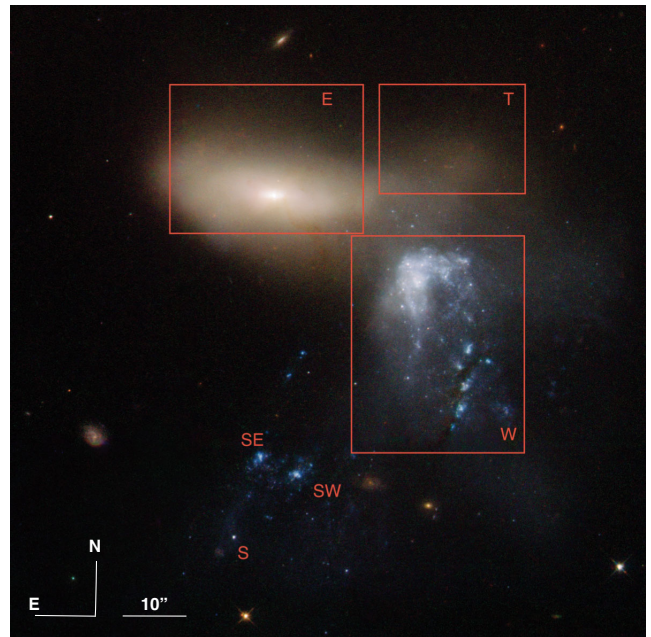


Figure 1. Colour composite image of the NGC 454 system obtained with *HST*-Wide Field Planetary Camera 2 in the *F450W* (*B*), *F606W* (*V*) and *F814W* (*I*) filter by Stiavelli et al. (1998). The figure highlights the different regions of the system following Johansson (1988) E and W areas including the early-type and the late-type member of the pair, respectively; S, SW and SE are knots likely connected to the W member. T is an area introduced by Stiavelli et al. (1998, see the text). The size of the FoV is 1.66 arcmin.

larger than 300 km s^{-1} and the $[\text{O III}] \lambda 5007 \text{ \AA}/\text{H}\beta$ ratio is larger than 3. However, none of the high-excitation lines expected in this case, as He II, were detected (see also Donzelli & Pastoriza 2000; Tanvuia et al. 2003). The AGN type of the nucleus has been recently detailed by Marchese et al. (2012). Their analysis of *Swift*, *XMM-Newton* and *Suzaku* observations characterizes the NGC 454 E nucleus as a ‘changing look’ AGN. This is a class of AGN showing significant variation of the absorbing column density along the line of sight.

The West region of the pair labelled in Fig. 1 as W (NGC 454 W hereafter) has been considered by Johansson (1988) as the debris of an irregular galaxy. However, the galaxy is so widely distorted by the ongoing interaction that the classification is difficult. Stiavelli et al. (1998) suggested that it is the debris of a disc galaxy. NGC 454 W is a starburst galaxy, as shown by the H α image of Johansson (1988, their figs 6a and b). The spectrum of NGC 454 W shows emission lines whose ratios, according to the above authors, are due to photoionization by star formation and shock heating.

The NGC 454 E region is particularly distorted in the North-West side. This region, labelled as T (NGC 454 T hereafter) in Fig. 1, has been studied by Stiavelli et al. (1998) which found that this is composed of a mix of the stellar populations of the NGC 454 E and the NGC 454 W. Moreover, they found a similarity between the colour of NGC 454 T region and that of the nearby sky and speculated about the presence of a faint tail of stripped material in this region not detected by the *HST* observations.

The picture of the NGC 454 system is completed by three blue knots, NGC 454 SW, NGC 454 SE and NGC 454 S, well detached from NGC 454 E, and likely connected to NGC 454 W (Johansson 1988; Stiavelli et al. 1998). Johansson (1988) suggested that these are newly formed globular clusters of $3 \times 10^6 M_{\odot}$ and $1\text{--}5 \times 10^7$ yr stellar age. Recently, several investigations suggest

Table 1. NGC 454 system basic properties from the literature.

| | | Ref. |
|---|---|-------|
| <i>NGC 454 E</i> | | |
| Morphology | E/S0 pec | (1,2) |
| RA (2000) | 1 ^h 14 ^m 25 ^s .2 | (3) |
| Dec. (2000) | −55° 23′ 47″ | (3) |
| V_{hel} | $3635 \pm 2 \text{ km s}^{-1}$ | (3) |
| $(B - V)_0$ | 0.80 | (1) |
| $(U - B)_0$ | 0.31 | (1) |
| L_X (0.1–0.3 keV) <i>XMM</i> | $2.8 \times 10^{39} \text{ erg cm}^{-2} \text{ s}^{-1}$ | (4) |
| L_X (0.1–0.3 keV) <i>Suzaku</i> | $5.6 \times 10^{39} \text{ erg cm}^{-2} \text{ s}^{-1}$ | (4) |
| L_X (0.1–0.3 keV) <i>XMM</i> | $2.5 \times 10^{42} \text{ erg cm}^{-2} \text{ s}^{-1}$ | (5) |
| L_X (0.1–0.3 keV) <i>Suzaku</i> | $7.2 \times 10^{42} \text{ erg cm}^{-2} \text{ s}^{-1}$ | (5) |
| L_X (14–150 keV) <i>XMM</i> | $4.8 \times 10^{42} \text{ erg cm}^{-2} \text{ s}^{-1}$ | (5) |
| L_X (14–150 keV) <i>Suzaku</i> | $1.4 \times 10^{42} \text{ erg cm}^{-2} \text{ s}^{-1}$ | (5) |
| <i>NGC 454 W</i> | | |
| Morphology | Irr (disrupted) Sp | (1,2) |
| RA (2000) | 1 ^h 14 ^m 20 ^s .1 | (3) |
| Dec. (2000) | −55° 24′ 02″ | (3) |
| V_{hel} | $3626 \pm 2 \text{ km s}^{-1}$ | (3) |
| $(B - V)$ | 0.32 | (1) |
| $(U - B)_0$ | −0.22 | (1) |
| $M(\text{H}_2)$ ($10^8 M_{\odot}$) | <2 | (6) |
| V_{hel} adopted (km s^{-1}) | 3645 | (7) |
| Distance (Mpc) | 48.5 ± 3.4 | (7) |
| Scale (kpc arcsec^{-1}) | 0.235 | (7) |

References: (1) Johansson (1988) provides the mean corrected radial velocity; the morphology is uncertain. (2) Stiavelli et al. (1998). (3) The heliocentric velocities of the E and W components are derived from Tanvuia et al. (2003) and are consistent with the systemic velocity $V_{\text{hel}} = 3645 \text{ km s}^{-1}$ provided by NED we adopted. (4) Valentina (private communication). (5) Marchese et al. (2012). (6) Horellou & Booth (1997). (7) The adopted heliocentric velocity and the distance (Galactocentric GSR) of the NGC 454 system are from NED.

that young independent stellar systems at $z \simeq 0$ start to form in tidal debris (see e.g. review by Lelli et al. 2015).

Table 1 summarizes some basic characteristics of NGC 454 E and W which appear as a prototype of an encounter/merger ($\Delta V_{\text{hel}} = 1 \pm 2 \text{ km s}^{-1}$; Tanvuia et al. 2003) between a late- and an early-type galaxy, the latter having an active and peculiar Seyfert-like nucleus. Therefore, the study of this system can make progress in our understanding of the effects of a wet interaction.

Our contribution consists of two correlated pieces of observational information: (1) the investigation of the multi-wavelength structure of NGC 454 E via the optical and UV surface photometry and (2) the analysis of the kinematics of the ionized gas component. The *Galaxy Evolution Explorer* (Morrissey et al. 2007) showed the strength of UV observations in revealing rejuvenation episodes in otherwise old stellar systems (see e.g. Rampazzo et al. 2007, 2011;

Marino et al. 2011, and references therein). In this context, we investigate the near-UV (NUV hereafter) stellar structure of the NGC 454 system using *Swift*-UVOT UV images (see also Rampazzo et al. 2017, and references therein). In order to study the ionized gas, connected to the ongoing star formation, we use the SOAR Adaptive Module (SAM) coupled with a Fabry–Perot to investigate its distribution, the 2D velocity and velocity dispersion fields of the $\text{H}\alpha$ emission in NGC 454 W and in NGC 454 SW and SE stellar complexes, likely debris of NGC 454 W. We finally attempt to derive the parameters and the merger history of the system using simulations.

The paper is organized as follows. In Section 2, we present *Swift*-UVOT (Section 2.1) and the SAM+Fabry–Perot (Section 2.2) observations of NGC 454 and the reduction techniques used. The *Swift*-UVOT surface brightness photometry is presented in Section 3. The ionized gas kinematics is presented in Section 4, the diagnostic diagrams of H II complexes are discussed in Section 5, while Section 6 considers the $\text{H}\alpha$ line profile decomposition. In Section 7, our results are discussed in the context of galaxy–galaxy interaction and compared with smoothed particle hydrodynamic (SPH) simulation with chemo-photometric implementation in Section 7.2. Finally in Section 8, we give the summary and draw general conclusion.

2 OBSERVATION AND DATA REDUCTION

2.1 *Swift*-UVOT observations

UVOT is a 30 cm telescope in the *Swift* platform operating both in imaging and spectroscopy modes (Roming et al. 2005). We mined the UVOT archive in the ASI Science Data Center retrieving the 00035244003 product including images of the NGC 454 system in all six filters available. Table 2 gives the characteristics of these filters, and calibrations are discussed in Breeveld et al. (2010, 2011).

The archival UVOT unbinned images have a scale of $0.5 \text{ arcsec pixel}^{-1}$. Images were processed using the procedure described in <http://www.swift.ac.uk/analysis/uvot/>. All the images taken in the same filter are combined in a single image using UVOT-SUM to improve the S/N and to enhance the visibility of NUV features of low surface brightness. The final data set of the *UVW2*, *UVM2*, *UVW1*, *U*, *B*, *V* images have total exposure times reported in Table 2.

UVOT is a photon counting instrument and, as such, is subject to coincidence loss when the throughput is high, whether due to background or source counts, which may result in an undercounting of the flux affecting the brightness of the source.

Count rates less than $0.01 \text{ counts s}^{-1} \text{ pixel}^{-1}$ are affected by at most 1 per cent and count rate less than $0.1 \text{ counts s}^{-1} \text{ pixel}^{-1}$ by at most 12 per cent due to coincidence loss (Breeveld et al. 2011, their fig. 6).

Table 2. *Swift*-UVOT integrated magnitudes.

| Filter | <i>UVW2</i> | <i>UVM2</i> | <i>UVW1</i> | <i>U</i> | <i>B</i> | <i>V</i> |
|-------------------------|------------------|------------------|------------------|------------------|------------------|------------------|
| Central λ | 2030 [Å] | 2231 [Å] | 2634 [Å] | 3501 [Å] | 4329 [Å] | 5402 [Å] |
| PSF (FWHM) | 2.92 arcsec | 2.45 arcsec | 2.37 arcsec | 2.37 arcsec | 2.19 arcsec | 2.18 arcsec |
| Zero-point ^a | 19.11 ± 0.03 | 18.54 ± 0.03 | 18.95 ± 0.03 | 19.36 ± 0.02 | 18.98 ± 0.02 | 17.88 ± 0.01 |
| Total exp. time | 1325 [s] | 2255 [s] | 3040 [s] | 652 [s] | 453 [s] | 762 [s] |
| Integrated magnitudes | [AB mag] | [AB mag] | [AB mag] | [AB mag] | [AB mag] | [AB mag] |
| NGC 454 E | 17.96 ± 0.13 | 17.83 ± 0.25 | 16.61 ± 0.28 | 15.15 ± 0.14 | 13.77 ± 0.18 | 13.20 ± 0.18 |
| NGC 454 W | 15.32 ± 0.15 | 15.16 ± 0.13 | 14.90 ± 0.09 | 14.46 ± 0.12 | 13.51 ± 0.20 | 13.13 ± 0.28 |

Note. ^aProvided by Breeveld et al. (2011) for converting UVOT count rates to AB mag (Oke 1974).

Coincidence loss effects can be corrected in the case of point sources (Poole et al. 2008; Breeveld et al. 2010). For extended sources, a correction process has been performed for NGC 4449, a Magellanic-type irregular galaxy with bright star-forming regions, by Karczewski et al. (2013). Even though their whole field is affected, the authors calculate that the statistical and systematic uncertainties in their total fluxes amount to ≈ 7 –9 per cent overall, for the NUV and the optical bands.

We checked, indeed, that in UV filters the coincidence losses may involve only few central pixels of the Irr galaxy, i.e. NGC 454 W, never exceeding 0.1 counts $\text{s}^{-1} \text{pixel}^{-1}$ (in particular, the maximum value of the count rates is 0.043, 0.028 and 0.047 counts $\text{s}^{-1} \text{pixel}^{-1}$ in *UVW2*, *UVM2* and *UVW1* filters, respectively). Our NUV images are very slightly affected so we decided not to account for this effect. Optical images are more affected. In the NGC 454 W region, the effect remains ≤ 0.1 counts $\text{s}^{-1} \text{pixel}^{-1}$ in all the bands; in particular, it reaches 0.09, 0.08 and 0.096 counts $\text{s}^{-1} \text{pixel}^{-1}$ in the *U*, *B* and *V* filters, respectively. As far as NGC 454 E is concerned, in the *U* filter count rates are at most 0.084 counts $\text{s}^{-1} \text{pixel}^{-1}$, and reach 0.2 in the *B* and *V* bands in the inner 5 arcsec. So, we add to the photometric error in Table 2 a further error of 12 per cent in optical bands to account for this effect.

We compared our total magnitudes in Table 2 with Prugniel & Héraudeau (1998) which reported a total magnitude of $B = 13.32 \pm 0.05$ and 13.44 ± 0.064 , respectively, for the whole NGC 454 system and for NGC 454 W. Once our measures are scaled to the Vega system ($B = B[\text{AB}] + 0.139$), we have $B = 13.43 \pm 0.15$ and 13.65 ± 0.12 , in very good agreement with previous estimates.

Our (*B* – *V*) colour, integrated within a 31 arcsec aperture and corrected for galactic absorption for NGC 454 E and NGC 454 W, is 0.88 ± 0.11 and 0.48 ± 0.06 , respectively, to be compared with 0.80 and 0.32 from Johansson (1988).

2.2 Fabry–Perot observation

Fabry–Perot (FP hereafter) observations¹ have been carried out on 2016 September 30 as part of the SAM-FP Early Science run at SOAR (Southern Astrophysical Research) 4.1 m telescope at Cerro Pachon (Chile). SAM-FP is a new instrument, available at SOAR, combining the adaptive optics SAM (Tokovinin et al. 2010a,b) and a scanning Queensgate ET70 etalon (Mendes de Oliveira et al. 2017). The SAM module has been conceived to deliver a 0.35 arcsec angular resolution across a 3 arcmin \times 3 arcmin field of view (FoV), depending on atmospheric condition, using ground layer adaptive optics. The SAM instrument detector is a 4K \times 4K CCD with a scale image scale of 0.0454 arcsec (physical pixel of 15 μ) on the sky (Fraga, Kunder & Tokovinin 2013). The present observations have been binned over 4 \times 4 pixels resulting in a scale of 0.18 arcsec pixel^{-1} . The interferometer used is an ET70 Queensgate scanning FP with an order of $p = 609@H\alpha$. The FP piezos are driven by a CS100 controller, positioned at the telescope. Table 3 gives the journal of observation with the characteristic of the etalon we used. At the centre of the free spectral range, we adopt the systemic velocity of 3645 km s^{-1} provided by NASA/IPAC Extragalactic Database (NED; see also Donzelli & Pastoriza 2000; Tanvuia et al. 2003, as more recent and independent sources).

¹ All FP data (cubes and moment maps) are available at cesam.lam.fr/fabryperot/, operated by Centre de Donnees Astrophysiques de Marseille at Laboratoire d’Astrophysique de Marseille.

Table 3. Instrumental setup.

| FP parameters | Values |
|---|--|
| Telescope | SOAR 4.1 m |
| Date | 2016 September 30 |
| Instrument | SAM-FP ^a |
| Detector | CCD |
| Pixel size (binned) | 0.18 arcsec pixel^{-1} (0.0454 arcsec \times 4) |
| Calibration neon light (λ) | 6598.95 Å |
| Resolution ($\lambda/\Delta\lambda$) | 10 700 |
| Filter characteristics | |
| Filter central wavelength | 6642 Å |
| Filter transmission | 80 per cent @ 6642 Å |
| Filter FWHM ($\Delta\lambda$) | 15 Å |
| Interferometer characteristics | |
| Interferometer order at $H\alpha$ | 609 |
| Free spectral range at $H\alpha$ (km s^{-1}) | 498 |
| Number of scanning steps | 43 |
| Sampling steps | 0.26 Å (11.60 km s^{-1}) |
| Total exposure time | 1.1 h (90 s/channel) |

^aTokovinin et al. (2010a,b).

Data have been reduced using home-made python macros to handle multi-extension files from SAM and building the data cube; some IRAF² specific tasks and ADHOCW³ software procedures have been used to handle the cube. The data reduction procedure has been extensively described by Amram et al. (1996) and Epinat et al. (2008). The first step, before the phase correction, is to perform the standard CCD data reduction by applying bias and flat-field corrections under IRAF as well as the cosmic removal using L.A.cosmic procedure (van Dokkum 2001). Linear combinations of dark images have been used to remove CCD patterns in different frames.

In addition to these canonical operations, it is necessary to check and correct for several effects, such as misalignment of data cube frames (due to bad guiding), sky transparency variation throughout the cube and seeing variation. Misalignment variation across the 43 frames of the data cube is less than half pixel; thus, it is negligible. The sky transparency has been corrected using a star in the FoV. It varies between 81 per cent and 98 per cent during the observation: each frame has been corrected accordingly using one channel as a reference. The same star is also used to map the corrected seeing variation ranging from 0.71 to 0.90 arcsec. We then applied a 2D spatial Gaussian smoothing equivalent to the worse estimated corrected seeing (0.90 arcsec). Phase map and phase correction have been performed using the ADHOCW package and by scanning of the narrow Ne 6599 Å line under the same observing conditions. The velocities measured are very accurate compared to the systemic velocity in Table 1, with an error of a fraction of a channel width (i.e. $< 3 \text{ km s}^{-1}$) over the whole FoV. The signal measured along the scanning sequence was separated into two parts: (i) an almost constant level produced by the continuum light in a 15 Å passband around $H\alpha$ (continuum map, not presented in this work) and (ii) a varying part produced by the $H\alpha$ line ($H\alpha$ integrated flux map). The continuum is computed by taking the mean signal outside the emission line. The $H\alpha$ integrated flux map was obtained by integrating the monochromatic profile in each pixel. The velocity sampling was 11.6 km s^{-1} . Strong OH night-sky lines passing through the filters

² IRAF is distributed by the National Optical Astronomy Observatories, which are operated by the Association of Universities for Research in Astronomy, Inc., under cooperative agreement with the National Science Foundation.

³ Available at <https://cesam.lam.fr/fabryperot/index/software>

were subtracted by determining the level of emission away from our target (Laval et al. 1987).

The velocity dispersion (σ hereafter) is derived from the determination of the full width at half-maximum (FWHM) from the determined profile. Then the real dispersion velocity is found supposing that different contributions follow a Gaussian function,

$$\sigma_{\text{real}}^2 = \sigma_{\text{obs}}^2 - \sigma_{\text{th}}^2 - \sigma_{\text{inst}}^2,$$

where $\sigma_{\text{inst}} = 12.82 \text{ km s}^{-1}$ is the instrument broadening deduced from the Ne calibration lamp and $\sigma_{\text{th}} = 9.1 \text{ km s}^{-1}$ is the thermal broadening of the H α line.

3 SURFACE PHOTOMETRY FROM SWIFT-UVOT OBSERVATIONS

The colour composite images in optical and NUV bands from the *Swift*-UVOT observations are shown in the top panels of Fig. 2. Images show that the NGC 454 W emission dominates in the NUV bands. In NUV, the NGC 454 W1–W6 complexes appear included in a unique envelope that elongates up to NGC 454 SW and SE. In NUV, two complexes, already revealed in H α by Johansson (1988), are projected between NGC 454 SE and NGC 454 W. NGC 454 S, shown in Fig. 1, appears connected to NGC 454 SW.

We derived the luminosity profiles and (*UVM2* – *V*) and (*B* – *V*) colour profiles of NGC 454 E. They are shown in the middle and bottom panels of Fig. 2. Luminosity profiles have been derived using the task *ELLIPSE* in the package *IRAF* (Jedrzejewski 1987). These are not corrected for galactic extinction. Since we aim at parametrizing the galaxy structure, we have truncated the profile at $\approx 35 \text{ arcsec}$ ($a^{1/4} = 2.43$) where the distortion by NGC 454 W, in particular in NUV, becomes dominant.

The (*B* – *V*) colour profile tends to become bluer with the galactocentric distance as shown in Stiavelli et al. (1998). The trend is much clear along the (*UVM2* – *V*) colour profile.

Stiavelli et al. (1998) parametrized the *HST* luminosity profiles with a composite bulge plus disc model. Due to our poorer resolution and point spread function (PSF), to parametrize the trend of optical and NUV surface brightness profiles, we adopt a Sérsic $r^{1/n}$ law (Sérsic 1968), widely used for early-type galaxies as a generalization of the $r^{1/4}$ de Vaucouleurs (1948) law (see e.g. Rampazzo et al. 2017, and references therein). We best fit a Sérsic law convolved with a PSF, using a custom *IDL* routine based on the *MPFIT* package (Markwardt 2009), accounting for errors in the surface photometry. The PSF model is a Gaussian of given FWHM, and the convolution is computed using Fast Fourier Transform on over-sampled vectors. We use the nominal value of the FWHM of the PSF of the UVOT filters. The residuals, $\mu - \mu_{\text{Sérsic}}$, are shown in two panels of Fig. 3, together with the values of the Sérsic indices for each of the UVOT bands reported in the top-right corner of the two panels. The Sérsic indices are in the range $1.09 \pm 0.13 \leq n \leq 1.79 \pm 0.06$.

We recall that the Sérsic law has three special cases: when $n = 1$, the value for an exponential profile, and $n = 0.5$, for a Gaussian luminosity profile and $n = 4$ for a bulge. The range of our Sérsic indices suggests that NGC 454 E has a disc. Residuals in Fig. 3 show a trend starting at about $a^{1/4} \simeq 1.6 \text{ arcsec}$ consistently with a clear change in colour in the (*UVM2* – *V*) colour profile.

4 IONIZED GAS MOMENT MAPS

We extract from SAM+FP observations the monochromatic H α emission map, the radial velocity and velocity dispersion maps. In

Fig. 4, we show *HST F450W* image (Stiavelli et al. 1998, top-left panel) on the same scale with our H α monochromatic map (bottom-left panel), heliocentric radial velocity map (top-right panel) and velocity dispersion map (bottom-right panel) of the system, corrected from broadening.

4.1 H α monochromatic intensity map

Both narrow-band imaging (Johansson 1988) and spectroscopy (Donzelli & Pastoriza 2000; Tanvuia et al. 2003) revealed H α emission in the NGC 454 system. The bottom-left panel of Fig. 4 shows the H α monochromatic intensity (*I*) map detected by our FP observations. H α emission is revealed in the nucleus of NGC 454 E, in the NGC 454 W region and in the NGC 454 SE and SW complexes. NGC 454 W region shows a structured H α emission. In this region, we spot six complexes we labelled from W1 to W6, roughly from North to South, as shown in Fig. 4 (bottom-left panel).

NGC 454 E has a type 2 Seyfert nucleus with broad, 250 and 300 km s^{-1} , emission profiles (Johansson 1988). That fits into the free spectral range of our etalon (almost 500 km s^{-1}). We apply a 5×5 pixel ($0.212 \times 0.212 \text{ kpc}$) boxcar smoothing to enhance the signal in the nuclear zone. The emission extends $3.3 \text{ arcsec} \times 2.0 \text{ arcsec}$ ($0.8 \text{ kpc} \times 0.7 \text{ kpc}$) around the centre of NGC 454 E. Integrating the signal within boxes (see Fig. 5) along the line connecting the NGC 454 E nucleus to the brightest complex of NGC 454 W (we labelled W1), we reveal emission lines whose profiles have complex shapes.

The W1 complex is the brightest in NGC 454 W, showing a nearly circular shape and a diameter of 5.7 arcsec (1.3 kpc); the W6 complex is the larger, extending to 8.5 arcsec (2 kpc). In the NUV map, we may distinguish all the W1–W6 complexes but they appear more extended and interconnected than shown by our FP observations.

The NGC 454 SW and NGC 454 SE emission complexes shown in Fig. 4 are relatively weaker than the W1–W6 complexes. We need to integrate the signal within 5×5 pixel bins to detect a connection between these complexes as shown in the Johansson’s H α narrow-band image. The bottom panels of Fig. 6 show emission-line profiles in several areas of NGC 454 W, NGC 454 SE and NGC 454 SW.

Both the H α image by Johansson (1988) and our NUV images show an elongated emission region between NGC 454 SW and NGC 454 W1 complex, weaker than the other regions. We also detect emission in between the SW, SE complex and the SW1 region (see Fig. 4). Our observation is showing a much smaller extension (1.1 arcsec corresponding to 0.3 kpc) compared to Johansson (1988).

To summarize, the W1–W6 as well as SW and SE in NGC 454 W are huge (up to 2 kpc wide) complexes of ionized interstellar medium (ISM hereafter). Ionized ISM is also found in NGC 454 E centre and along the line connecting it to the NGC 454 W1 complex.

4.2 Radial velocity map

Fig. 4 (top-right panel) shows the 2D radial velocity, V_r , map of NGC 454. NGC 454 E velocity field is difficult to interpret because this object is an AGN showing large line profiles, almost covering our free spectral range. Nevertheless, a velocity gradient of 130 km s^{-1} , across 4 arcsec (0.94 kpc), is measured.

Velocities in the NGC 454 W range over 70 km s^{-1} , from a maximum of 3645 km s^{-1} measured in the W2 complex to a minimum of

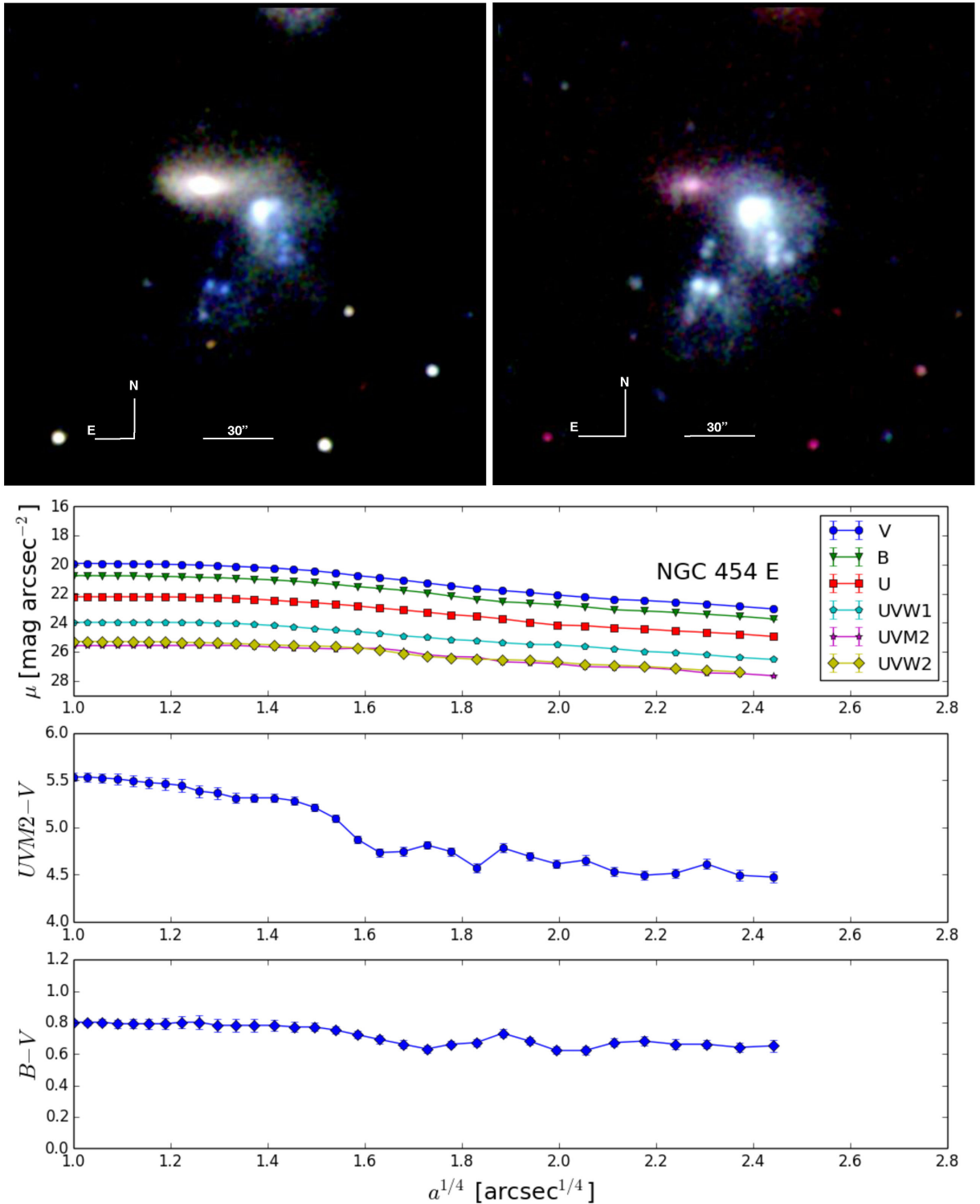


Figure 2. Top panels: optical image (U -blue, B -green, V -red), on the left, and UV colour composite image ($UVW2$ -blue, $UVM2$ -green, $UVW1$ -red), on the right, of the NGC 454 system as observed by *Swift* UVOT. The images have been smoothed 2×2 pixels (resulting in $1 \text{ arcsec} \times 1 \text{ arcsec}$ resolution). The total field of view is $4 \text{ arcmin} \times 4 \text{ arcmin}$. Middle panel: luminosity profiles of NGC 454 E in the optical and NUV bands. Profiles are not corrected for coincidence loss and galactic absorption. Bottom panels: ($M2 - V$) and ($B - V$) colour profiles in [AB] magnitudes corrected for galactic absorption.

3575 km s^{-1} in the southern tip of W6 complex. None of the W1–W6 complexes has a rotation pattern. The W6 complex shows a velocity gradient of 35 km s^{-1} across a length of 8.3 arcsec (1.95 kpc). The NGC 454 SW and NGC 454 SE complexes do not present veloc-

ity gradients. With respect to the W1–W6 complexes, the SW and SE complexes are receding with a systemic velocity of 3725 and 3691 km s^{-1} , respectively, with a velocity difference $\Delta V \simeq 115$ – 145 km s^{-1} with respect to the W1 complex.

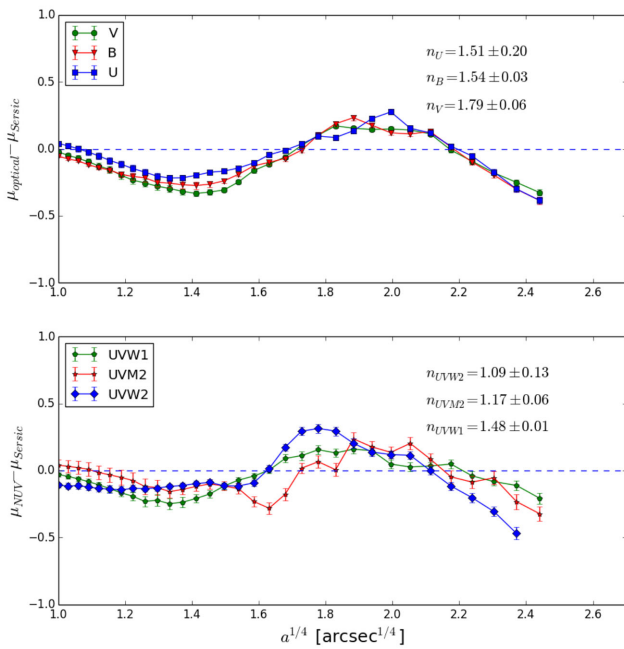


Figure 3. Residual from the fit of a single Sérsic $r^{1/n}$ law of the optical (top panel) and NUV (bottom panel) luminosity profiles. The values of the Sérsic indices, for each UVOT band, are reported on the top-right side of the figure. The values of the indices suggest the presence of a disc structure.

4.3 Velocity dispersion map

The velocity dispersion, σ , map is shown in the bottom-right panel of Fig. 4. As mentioned before, NGC 454 E shows very broad profiles, very close to our free spectral range. In those conditions, we prefer not to show a velocity dispersion map for this galaxy. We measure σ values ranging from 14 to 42 km s⁻¹ in the W3, W4, W5, W6 complexes. σ values of NGC 454 SW and NGC 454 SE are homogeneous, between 20 and 29 km s⁻¹. We point out that values exceeding 10–20 km s⁻¹ indicate supersonic motions (see e.g. Smith & Weedman 1970). The W1 complex shows the highest values, up to 66 km s⁻¹, while in the W2 complex, σ ranges from 13 to 32 km s⁻¹.

4.4 Emission between H II regions

Figs 5 and 6 show several regions in between NGC 454 E and NGC 454 W1 (Fig. 5), NGC 454 SW and NGC 454 SE (Fig. 6, top) and between NGC 454 W3, W4, W5 and W6 (Fig. 6, bottom).

Fig. 5, regions 1 and 2, shows the emission centred in the elliptical. As mentioned before, the centre of NGC 454 E has a broad emission as shown in region 2. With an emission peak above 3800 (in relative units) and a background of 2500, region 2 has a very high intensity considering that background is dominated by Poisson noise and even if we consider that the profile has an FWHM of 300 km s⁻¹ (compared to the 500 km s⁻¹ of the free spectral range), we still see the emission of the centre of the elliptical. Regions 3 and 4 show areas in between NGC 454 E and NGC 454 W1; when region 3 shows a comfortable emission line, region 4 shows the limit of our detection with an emission peak at 1σ above the continuum level. Regions 5 and 6 show NGC 454 W1 emission; a detailed discussion about this is given in Sections 5.2 and Section 6.

Fig. 6 (top) shows emission profiles between the SE and SW regions. Emission is very clear across both regions. No substantial

velocity gradient is visible even if the radial velocity of SW is 30 km s⁻¹ lower than SE.

Fig. 6 (bottom) shows the connection between the remaining regions (NGC 454 W3 to W6). Emission is strong, and it is clear that all regions are connected. Zones 1 and 12 show asymmetric profiles, probably due to a second component. A radial velocity gradient is visible between the southern tip with zone 5 and region 1.

5 H II REGIONS DIAGNOSTIC DIAGRAMS

5.1 Description of the complexes

Complexes in NGC 454 W share similar dynamical characteristics both with giant H II regions (GH II Rs) and the so-called H II galaxies. First, like GH II Rs, W1 has high supersonic profiles (Smith & Weedman 1970) and, secondly, the high velocity dispersion surrenders high monochromatic emission. Several studies using FP interferometer (Muñoz-Tuñón, Tenorio-Tagle & Castañeda 1996) found this signature in nearby GH II R, like NGC 604. More recently, still using FP and Integral Field Unit spectroscopy, Bordalo, Plana & Telles (2009), Moiseev & Lozinskaya (2012) and Plana & Carvalho (in preparation), pieces of evidence have been found of such signature within dwarf H II galaxies.

Fig. 7 considers three different diagnostic diagrams used to study the kinematics of H II regions. These diagnostic diagrams are shown for NGC 454 W complexes (W1–W6 identified in Fig. 4) and for NGC 454 SW and SE regions.

The W1 complex has the larger intensity range. We will discuss the $(I - \sigma)$ regimes in this region in Section 5.2 with a statistical approach.

The panels (a) in Fig. 7 represent the intensity versus the dispersion velocity (sigma). The W2–W6 as well as SW1, SW2 and SE complexes show similar intensity and sigma ranges. In W3–W6 as well as NGC 454 SW and SE complexes, the scatter of σ increases as the intensity decreases. As discussed by Moiseev & Lozinskaya (2012, their fig. 6), this shape is produced within star-forming complexes with significant excursion of gas densities, indicating low-density, turbulent ISM. In high-density (high-intensity) regime, H II regions have either nearly constant or low-scatter σ . However, towards lower density (low intensity), the high perturbed/turbulent gas surrounding H II regions may emerge so decreasing the intensity of the σ scatter may increase. We have separated the different regions: W3, W4, W5 and W6 as SE, SW1 and SW2 complexes in these diagrams. The last row of Fig. 7 shows the SE, SW1 and SW2 complexes' I versus σ diagram, but none of the three complexes shows a different pattern. Introduced by Muñoz-Tuñón et al. (1996), the $(I - \sigma)$ diagram has been used by those authors to identify expanding shells by localizing inclined bands. This interpretation is based on the fact that the velocity dispersion should be higher at the centre of the shell and the intensity lower because less material is crossed along the line of sight than at the shell inner and outer edges. Assuming this pattern, the inclination of the band can also be interpreted in terms of age of the shell itself. As the shell ages, the velocity dispersion at the centre decreases as well as the intensity difference between the centre and inner edge of the shell (see fig. 3 in Muñoz-Tuñón et al. 1996). The Moiseev & Lozinskaya (2012) interpretation tends to act for larger scales, where high velocity dispersion is not related to specific expanding shells, but rather belong to the diffuse low brightness emission.

The panels (b) in Fig. 7 represent the intensity versus radial velocity ($I - V_r$) diagram of the W1–W6 complexes in NGC 454 W, and in the SW1, SW2 and SE.

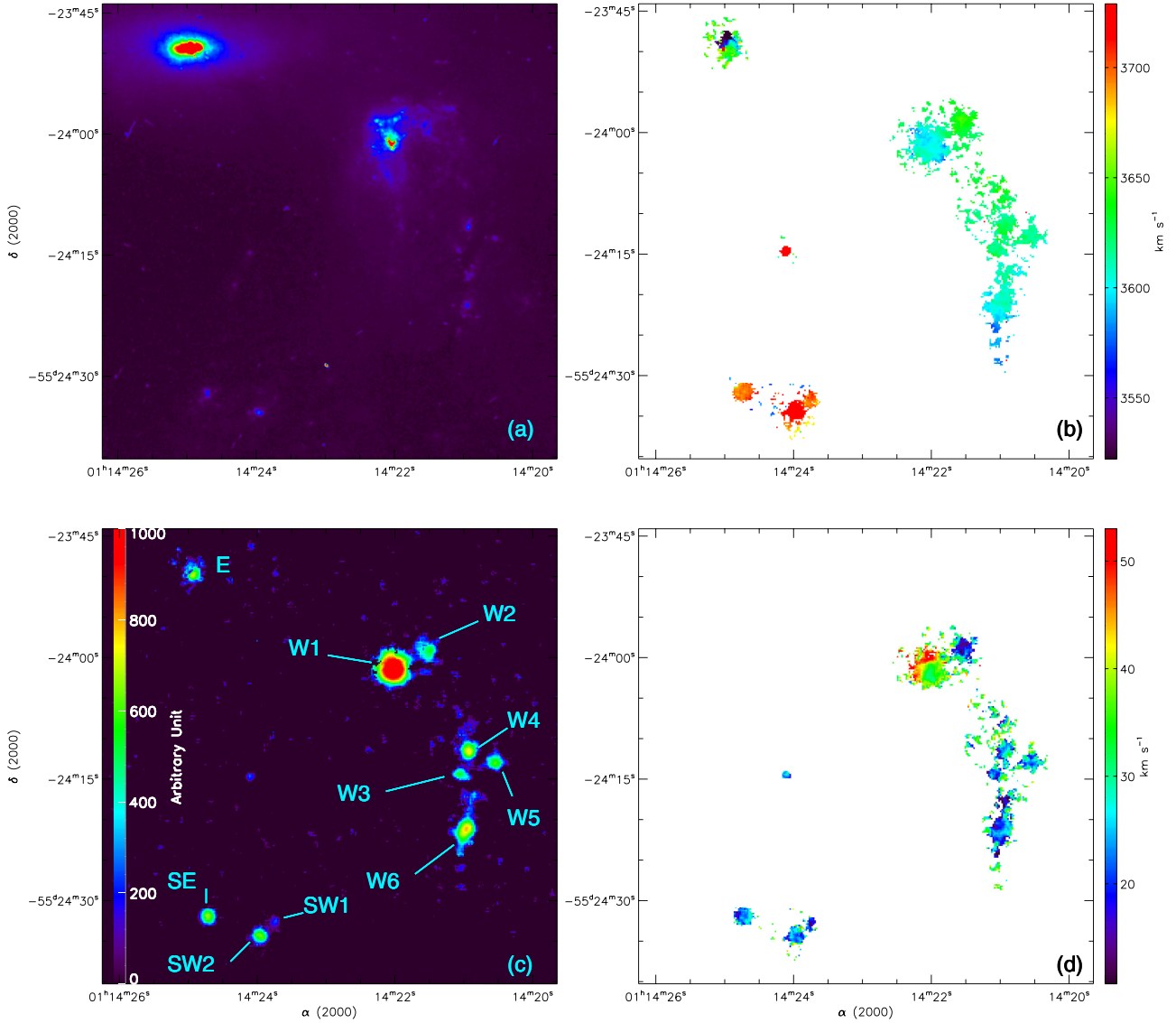


Figure 4. (a) *HST* F450W image of the NGC 454 system (Stiavelli et al. 1998), (b) 2D velocity field of H α emission, centred on the NGC 454 systemic velocity, (c) monochromatic H α map and (d) H α velocity dispersion map, corrected from broadening.

The range of radial velocity, V_r , within complexes is small, of the order of 20–40 km s $^{-1}$ in the W3–W6 and NGC 454 SW1, SW2 and SE complexes. Large radial velocity excursion at all intensities is found in W2. The W3, W4, W5 and W6 complexes show different radial velocities, with W4 having the highest and W6 the lowest. W6 velocity range is larger because of the velocity gradient we already mentioned in Section 4. The separation in radial velocity between the SE, SW1 and SW2 complexes is shown in the plot (b) of the last row of Fig. 7. The NGC 454 SE, SW and SW2 complexes have a small variation, 10–20 km s $^{-1}$, of V_r while the monochromatic intensity range is similar to the W3–W6 complexes. It also appears that the SW1 complex has a closer radial velocity with SE than with SW2. According to Bordalo et al. (2009, their fig. 13b), a vertical band in this diagram, representing a velocity variation in a short intensity range, means a radial motion such as an expansion, but it could also mean an inflow. The physical mechanisms in action are several including turbulence, winds, flows, bubbles or the self-gravity of the complexes at different scales. Even if a vertical band

can appear in the plot representing W2 (second row), it is difficult to interpret it as a signature of a radial motion, the intensity range being too wide.

The panels (c) in Fig. 7 consider the $(V_r-\sigma)$ diagrams in the same regions. Bordalo et al. (2009) pointed out that a dependence between the variables may indicate systematic relative motion of the clouds in the complex. They presented an idealized pattern for this diagram. Inclined $(V_r-\sigma)$ patterns would represent systematic motion like champagne flows such that cloud of gas with high σ moves away from us (positive slope) or towards us (negative slope).

We perform a standard Pearson’s product-moment correlation test for the different complexes of NGC 454, in order to show the existence of systematic motions mentioned above. Except for W1 and SW1, all regions show a weak-to-moderate correlation, according to this test. W2 has a correlation coefficient of -0.34 , W3 of -0.43 , W4 of -0.23 , W5 of -0.27 and W6 of -0.17 . The SE and SW2 regions also have a weak-to-moderate correlation with coefficients of 0.48 and -0.25 , all of them with a 99.9 per cent confidence

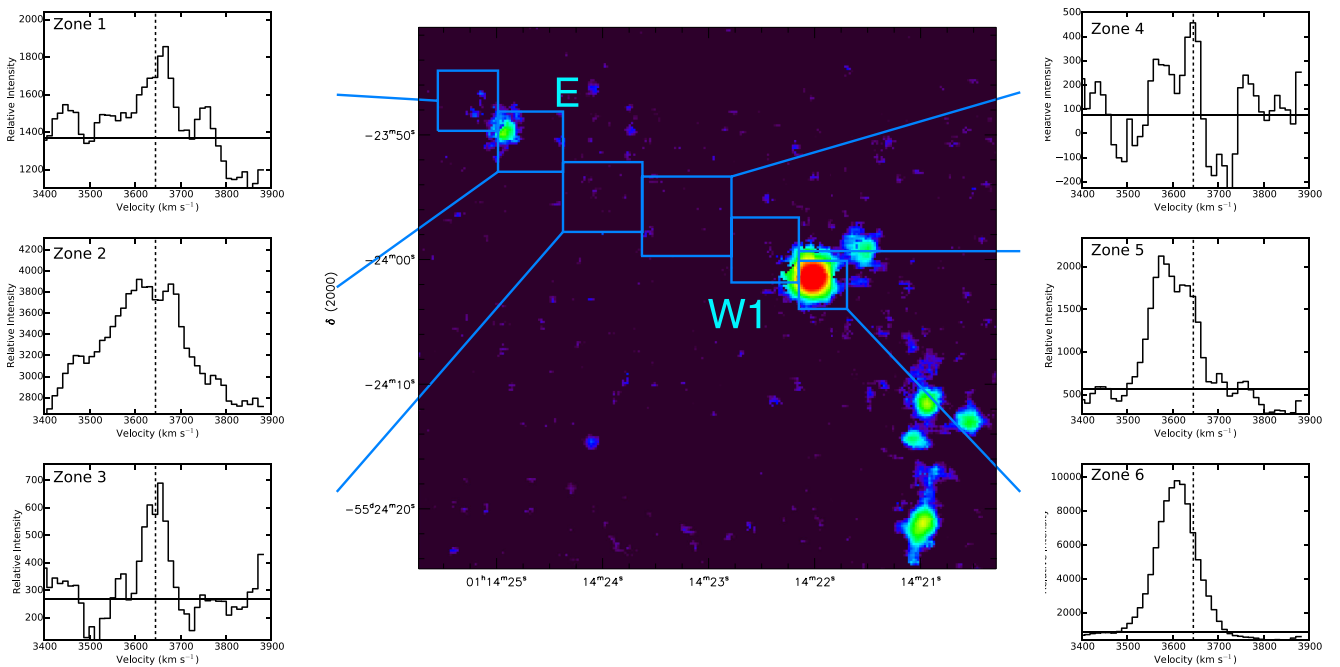


Figure 5. Emission profiles in the region NGC 454 E and NGC 454 W1. The vertical dotted line indicates the adopted systemic velocity $V_{\text{hel}} = 3645 \text{ km s}^{-1}$. The horizontal line indicates the mean continuum level. The map corresponds to the monochromatic emission.

level. The case of SW1 is a bit more complex. The Pearson test is not conclusive, and we decide to use a robust correlation test in order to put lower weight in marginal points. Using the `wrs2` package in R, we found a correlation of -0.2 with a 90 per cent confidence level.

We perform a simple linear regression [the solid line in Fig. 7, panels (c)] for the regions where the Pearson test shows a weak-to-moderate correlation: W2 to W6, SE and SW2. In this context, W2 and SW2 regions can be interpreted as complexes with relatively high dispersion, moving towards the observer (negative slope). In the case of the SE complex, the slope is positive and it can be interpreted as a complex moving away from the observer.

Previous studies, on GH nR or emitting dwarf galaxies, also used those diagnostic diagrams when these objects are smaller and the scale resolution much smaller than here. For example, NGC 604 from Muñoz-Tuñón et al. (1996) or dwarf galaxies from Moiseev & Lozinskaya (2012) or Bordalo et al. (2009) have, respectively, scale resolutions of 3.31 and 21 pc arcsec $^{-1}$. This is 10 times smaller than our object, although we found remarkable similarities between diagnostic diagrams.

5.2 Statistical analysis of the (I - σ) diagrams for W1 complex

We use the R statistical package.⁴ R is largely used in different statistical analysis. The `Mclust` routine has only been recently used in astrophysics by Einasto et al. (2010) to detect structure in galaxy clusters. We aim at finding how many independent components are

⁴ R Development Core Team, under the `distrEx` (Ruckdeschel et al. 2006). R is an open-source free statistical environment developed under the GNU GPL (Ihaka & Gentleman 1996). Available at: <http://www.rproject.org> to analyse the (I - σ) diagram of the W1 complex.

present (task `Mclust`), to locate them in the diagram and in the σ map (so-called geographic location). `Mclust` is an R function for model-based clustering, classification and density estimation based on finite Gaussian mixture modelling. An integrated approach to finite mixture models is provided, with routines that combine model-based hierarchical clustering and several tools for model selection (see Fraley & Raftery 2007).

For a bivariate random sample \mathbf{x} be a realization from a finite mixture of $m > 1$ distributions, it should follow

$$p(\mathbf{x}|\pi, \{\mu_k, \Sigma_k\}) = \sum_k \pi_k \phi(\mathbf{x}|\mu_k, \Sigma_k), \quad (1)$$

where ϕ is the multivariate normal density

$$\phi(\mathbf{x}|\mu, \Sigma) = (2\pi)^{-d/2} |\Sigma|^{-1/2} \exp \left\{ -\frac{1}{2} (\mathbf{x} - \mu)' \Sigma^{-1} (\mathbf{x} - \mu) \right\}, \quad (2)$$

$\pi = \{\pi_1, \dots, \pi_m\}$ are the mixing weights or probabilities (such that $\pi_k > 0$ and $\sum_k \pi_k = 1$), (μ_k, Σ_k) are the mean of the covariance matrix of the component k and d is the dimension of the data. A central question in finite mixture modelling is how many components should be included in the mixture. In the multivariate setting, the volume, shape and orientation of the covariances define different models (or parametrization) with their different geometric characteristics. In `Mclust`, the number of mixing components and the best covariance parametrization are selected using the Bayesian information criterion. The task outputs μ_k, Σ_k and π_k for k running from 1 to m . `Mclust` also relates each element in the data set to a particular component in the mixture. To gain some flexibility on this classification, we combine the central result of `Mclust`, the number of components m , with the result of another R task: the `mvnormalmixEM` function.

This task belongs to the `MIXTOOLS` package, which provides a set of functions for analysing a variety of finite mixture models. The

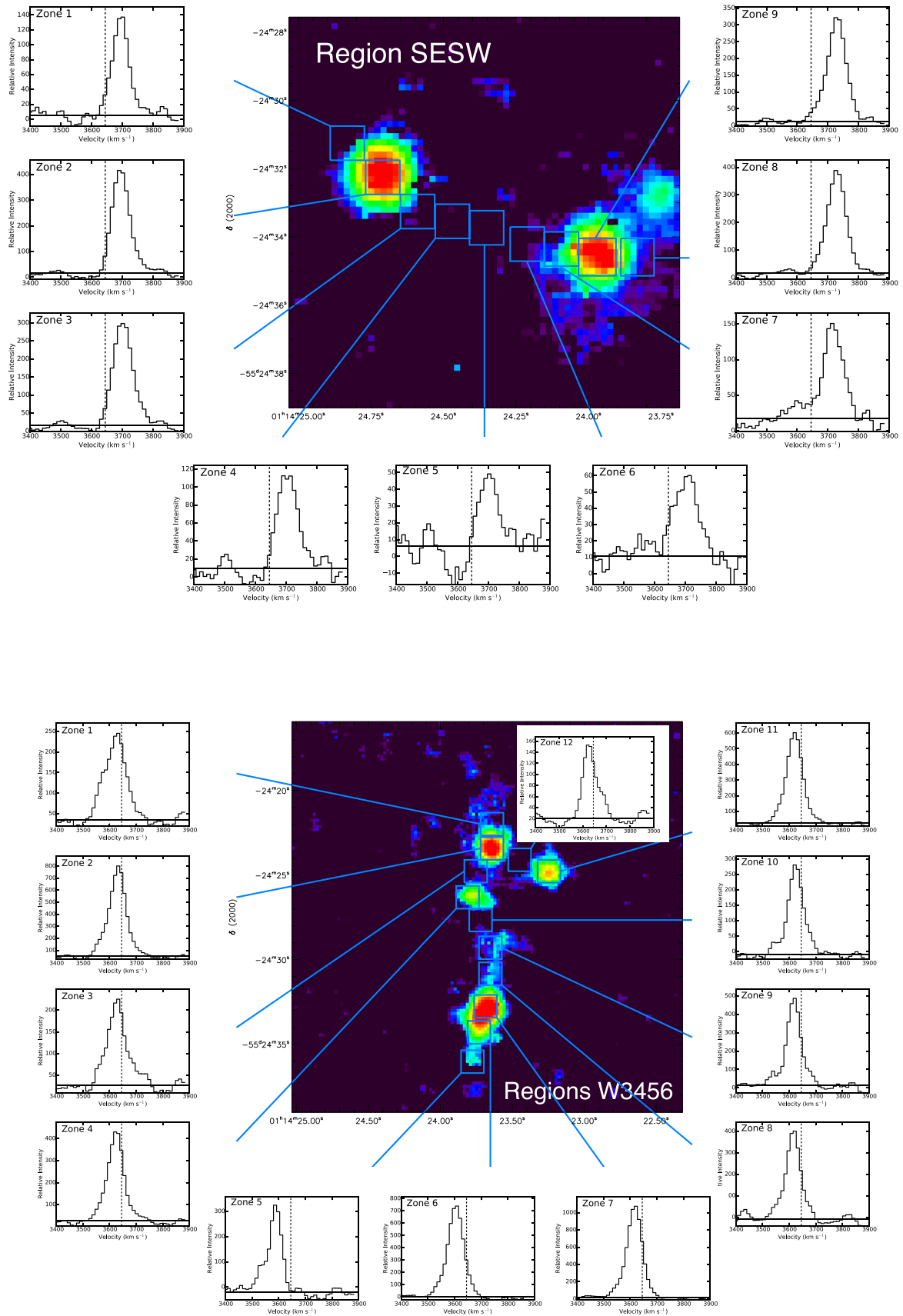


Figure 6. Emission profiles in NGC 454 SE and NGC 454 SW (top panel) and in the NGC 454 W region between the W3 and W6 complexes (bottom panel). The vertical dotted line indicates the adopted systemic velocity $V_{\text{hel}} = 3645 \text{ km s}^{-1}$. The horizontal line indicates the mean continuum level. The map corresponds to the monochromatic emission.

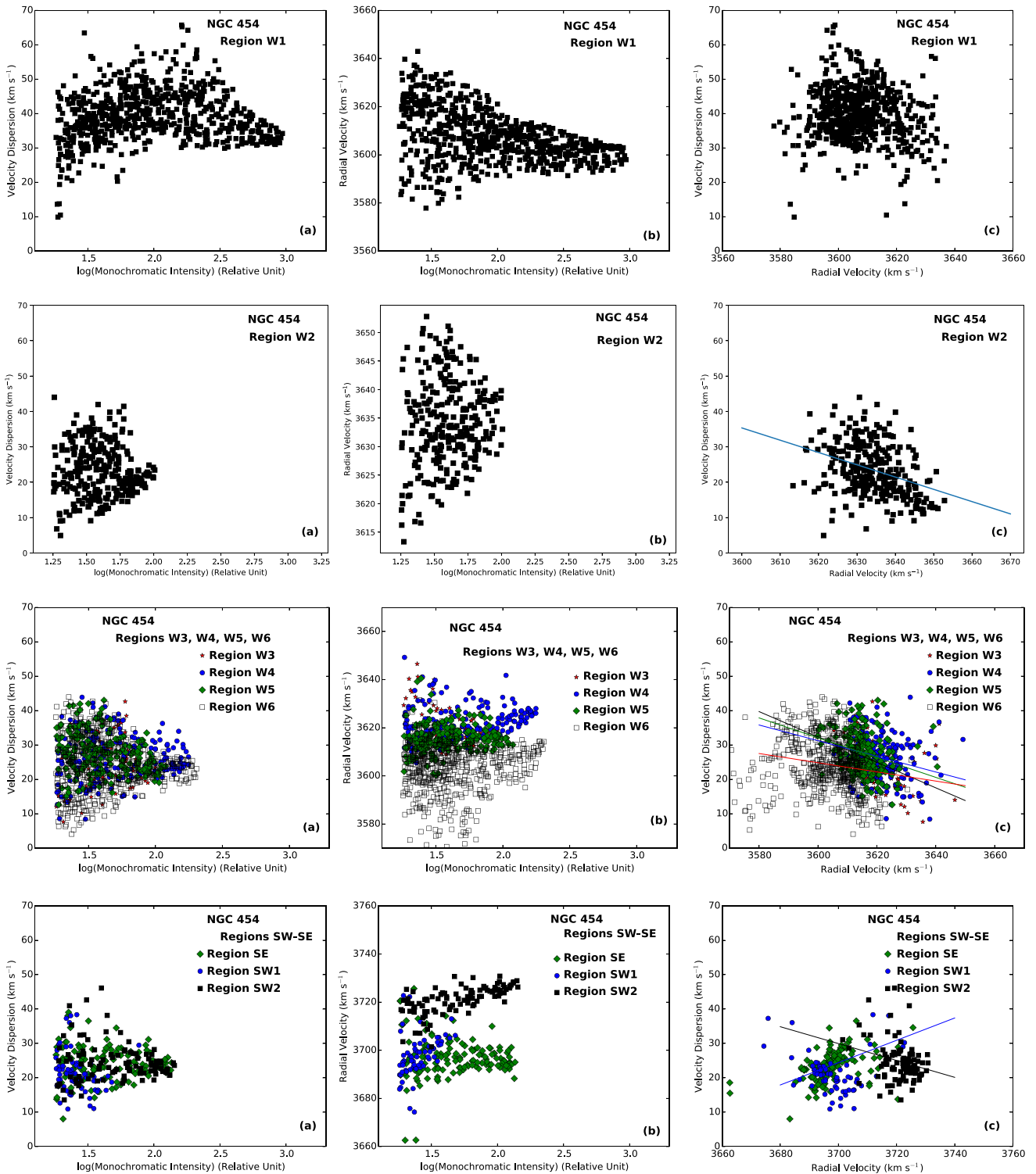


Figure 7. From top to bottom: panels (a) ($I-\sigma$), panels (b) ($I-V_r$), panels (c) ($V_{\text{hel}}-\sigma$) diagnostic diagrams in the W1–W6 complexes in NGC 454 W and in the NGC 454 SE and SW complexes. The plot results from a single Gaussian fit to the line profile. Solid lines in $V_r-\sigma$ diagrams represent the linear regressions applied when Pearson’s correlation test is robust.

general methodology used in MIXTOOLS involves the representation of the mixture problem as a particular case of maximum likelihood estimation when the observations can be viewed as incomplete data. The code uses the expectation–maximization algorithm that maxi-

mizes the conditional expected log-likelihood at each M-step of the algorithm – see details in Benaglia et al. (2009). The code returns the posterior probabilities for each observation with respect to the m different components.

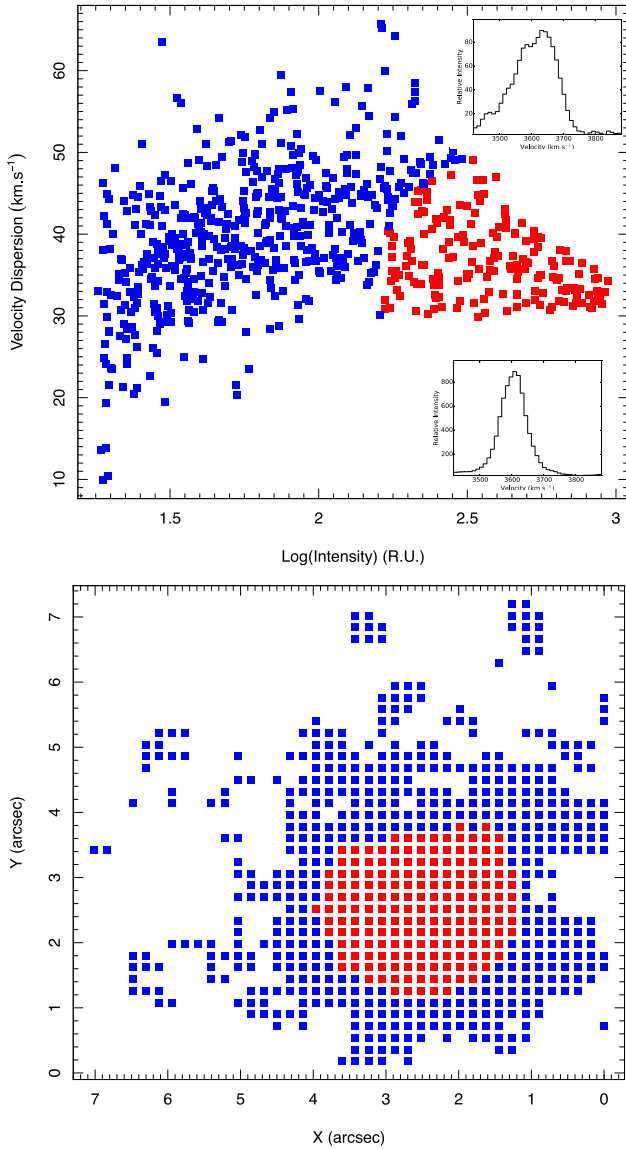


Figure 8. Bottom panel: the 3×3 pixel sampling of the NGC 454 W1 complex. Top panel: $(I-\sigma)$ plot. The colours highlight two regions, the central and outskirts, with different regimes (see Section 5.2 for details). The top profile shows a typical monochromatic emission representative of the blue points, and the bottom profile representative of the red points.

Since running `Mclust` results in $m = 2$ components, we then use the task `mvnormalmixEM`, looking at two independent classes with 80 percent confidence in the $(I-\sigma)$ maps. Once these two classes have been found, we have represented them in the $(I-\sigma)$ diagram (Fig. 8, upper panel) and in the σ map (Fig. 8, lower panel). The figure clearly shows the two regions, one in the centre (low dispersion and strong emission) and the other surrounding it (high dispersion and low emission). W1 is an extended ionized ISM complex so we cannot easily apply the interpretative scheme of H II regions. We may exclude the fact that W1 may be interpreted as an expanding wind-blown bubble that would have a different signature in a $(I-\sigma)$ map: σ values should decrease from the centre to the edge of the shell, according to Lagrois & Joncas (2009). The two regimes evidenced by the statistical approach support the picture proposed by Moiseev & Lozinskaya (2012) in which the W1 complex can be viewed as composed of a giant dense H II region in the central part and turbulent low-density gas cloud in its outskirts.

6 H α LINE PROFILE DECOMPOSITION

Fig. 4 (bottom-right panel) shows the large range of σ in the W1 complex with respect to the other complexes in NGC 454 W as well as in the NGC 454 SW and SE. Fig. 5 shows that emission lines are quite broad so that the high velocity dispersion in the W1 complex can be attributed to the presence of multiple components in the emission profiles. Fig. 9 shows line profiles resulting from the mapping of the W1 and W2 complexes.

We perform a Gaussian decomposition of the 14 H α line profiles (13 in W1 and one in W2 as a sort of control field) shown in Fig. 9. Each region represents a 3×3 pixel box ($0.54 \text{ arcsec} \times 0.54 \text{ arcsec}$ area, $0.13 \times 0.13 \text{ kpc}$). The decomposition has been performed using a home-made program with three different Gaussian components. We first fit the brightest component, subtract it and then fit the two others, until the final fit converges. Fig. 9 shows the decomposition of these profiles and the location of areas in W1 and W2. Table 4 lists the characteristics of the three Gaussian components ordered by decreasing intensity component.

We are aware that a simple mathematical approach is always unsatisfactory; since the composition is not unique, but linked to a physical and kinematical interpretation, we are reasonably satisfied with the result.

Considering the results of the decomposition reported in Table 4, shown in Fig. 9, we draw the following conclusions.

The central region, labelled W1 7, has a symmetrical profile when compared to all the other regions. The σ of the brightest Gaussian component of W1 complex has supersonic values between 20 and 25 km s^{-1} . The σ of the main component of all regions in W1 is larger than in W2.

With respect to the systemic velocity, the main Gaussian component in W1 [1 to 5] is redshifted while in the zones of W1 [9 to 11] it is blueshifted, sketching a sort of rotation pattern being at the opposite sides of the W1 complex centre. We can also note that positions of the second component with respect to the main one (second redshifted component at one side of the W1 complex and the second blueshifted component at the other side) could be seen as a bipolar outflow due to massive star formation.

Several zones of W1 clearly show profiles with an apparent second component (e.g. W1 1, W1 2, W1 3, W1 4 and W1 6), while, in general, the other zones, including the W2 zone, need fainter components to fit the wings of the line profiles.

We conclude that even with multiple Gaussian fit analysis no unambiguous rotation pattern emerges in the W1 complex.

Using the characteristics of the Gaussian decomposition resumed in Table 4, we present, in Fig. 10, a revised $(I-\sigma)$ diagnostic diagram, showing the $(I-\sigma)$ diagram for the main, i.e. the brightest, component. In Fig. 10, top panel, we present the mean σ per intensity bin. The associated error bar represents the standard deviation in the bin. The red points represent the intensity and σ of the main component (see component 1 in Table 4). As mentioned before, σ is significantly lower, still largely supersonic and similar, on average, to regions W2–W6, and SE–SW shown in the bottom panel of Fig. 10. However, the σ of the main component in W1 shows a positive slope with I .

7 DISCUSSION

7.1 NGC 454: general view

In the NGC 454 system, there is no evidence of a velocity difference between the two members. The pair is furthermore strongly isolated as discussed in Appendix A. Our observations do not provide direct evidence of gas re-fuelling of NGC 454 E on the part

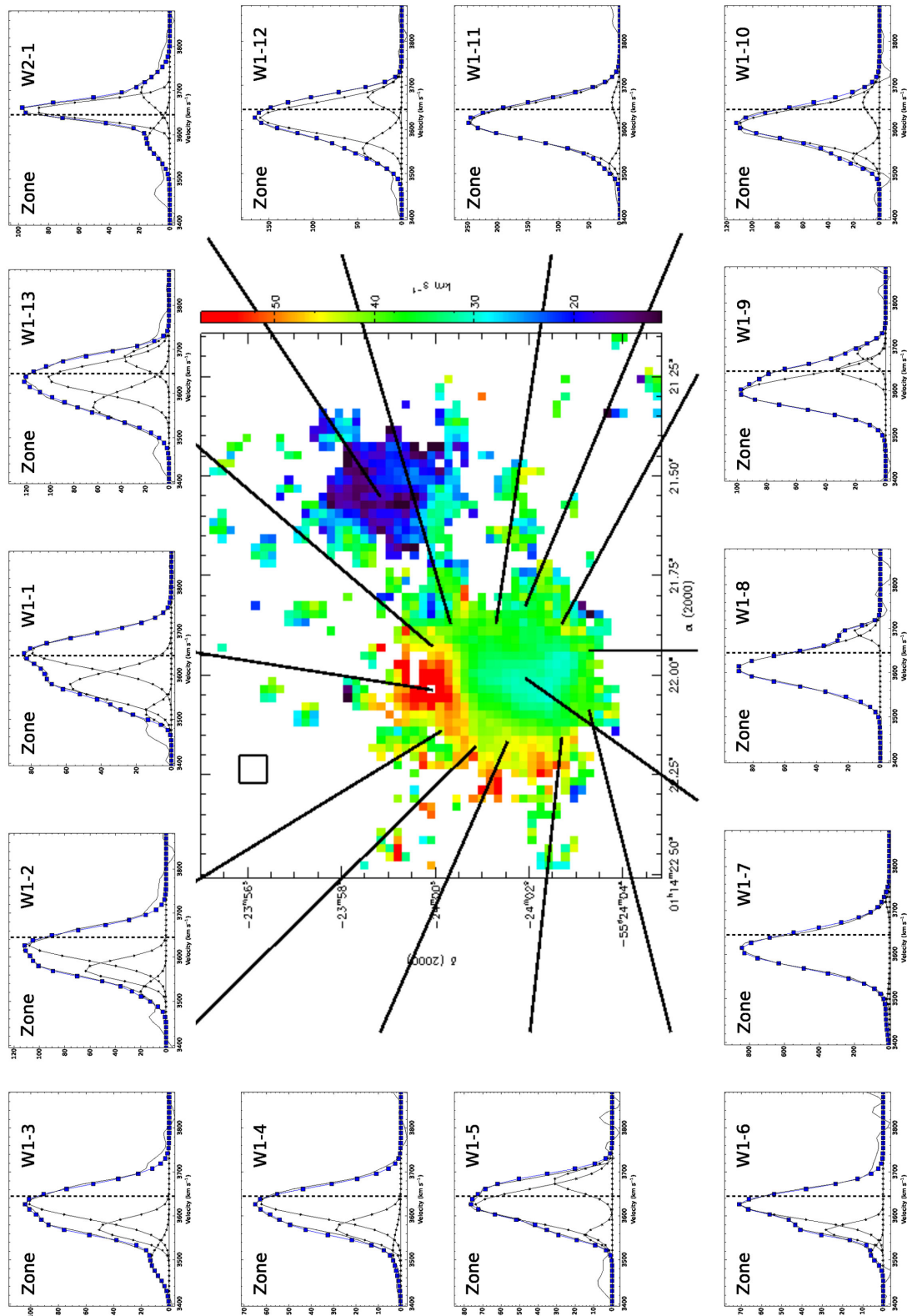


Figure 9. Integrated profiles in NGC 454 W1 and W2. Three Gaussian component fit of the emission lines in NGC 454 W1 and W2 complexes. Results of the fitting are reported in Table 4. The vertical dotted line indicates the adopted systemic velocity $V_{hel} = 3645$ km s⁻¹. The horizontal line indicates the mean background level. The small square approximately represents the size of the area of the integrated profiles (3×3 pixels or 0.54 arcsec). The map corresponds to the dispersion velocity field, corrected from broadening.

Table 4. H α line profiles of Gaussian components in region W1. The intensity, I (columns 2, 5 and 8), is in relative units (R.U.).

| Regions (1) | Component 1 | | | Component 2 | | | Component 3 | | |
|----------------|----------------------|---------------------------------|------------------------------------|----------------------|---------------------------------|------------------------------------|----------------------|---------------------------------|-------------------------------------|
| | I (R.U.) (2) | V_r (km s $^{-1}$) (3) | σ (km s $^{-1}$) (4) | I (R.U.) (5) | V_r (km s $^{-1}$) (6) | σ (km s $^{-1}$) (7) | I (R.U.) (8) | V_r (km s $^{-1}$) (9) | σ (km s $^{-1}$) (10) |
| Region W1 1 | 80.0 | 3654 | 22.2 | 58.0 | 3577 | 19.7 | 15.0 | 3516 | 11.3 |
| Region W1 2 | 108.0 | 3629 | 20.7 | 64.0 | 3572 | 13.8 | 20.0 | 3522 | 13.8 |
| Region W1 3 | 102.0 | 3632 | 22.2 | 51.0 | 3572 | 13.8 | 13.0 | 3499 | 21.2 |
| Region W1 4 | 063.0 | 3632 | 20.7 | 29.0 | 3572 | 4.8 | 03.5 | 3522 | 27.1 |
| Region W1 5 | 74.0 | 3624 | 22.2 | 32.0 | 3679 | 13.8 | 15.0 | 3557 | 09.9 |
| Region W1 6 | 71.0 | 3627 | 18.7 | 28.5 | 3566 | 9.9 | 6.0 | 3514 | 10.1 |
| Region W1 7 | 662.0 | 3611 | 24.6 | 25.0 | 3487 | 26.6 | 20.0 | 3725 | 22.1 |
| Region W1 8 | 90.0 | 3609 | 22.6 | 16.5 | 3693 | 7.9 | 0.0 | 3383 | 00.0 |
| Region W1 9 | 98.0 | 3596 | 21.2 | 33.0 | 3647 | 10.9 | 19.0 | 3687 | 12.9 |
| Region W1 10 | 110.5 | 3610 | 21.2 | 21.0 | 3534 | 12.3 | 13.0 | 3661 | 16.8 |
| Region W1 11 | 245.5 | 3617 | 24.6 | 18.0 | 3516 | 12.3 | 13.0 | 3661 | 16.8 |
| Region W1 12 | 160.0 | 3627 | 20.7 | 44.0 | 3555 | 18.7 | 38.0 | 3673 | 12.4 |
| Region W1 13 | 102.0 | 3635 | 19.7 | 64.0 | 3572 | 21.7 | 38.0 | 3680 | 13.8 |
| Region W2 1 | 90.0 | 3656 | 12.3 | 19.0 | 3690 | 19.7 | 15.0 | 3586 | 20.7 |

of NGC 454 W. We found, however, traces of ionized gas beyond the nucleus as shown in Fig. 5. We detect broad emission line in the NGC 454 E nucleus but the small free spectral range prevents us to disentangle the presence of multiple components, which may provide us information about possible gas infall (see e.g. Rampazzo et al. 2006; Font et al. 2011; Zaragoza-Cardiel et al. 2013, and references therein). However, a velocity gradient of about 130 km s $^{-1}$ has been revealed in the central 4 arcsec. *Swift*-UVOT observations of NGC 454 E suggest that the galaxy is an S0 since a disc emerges in all the UVOT bands when a Sérsic law is fitted to the luminosity profile. Both the $(B - V)$ and $(M2 - V)$ colour profiles become bluer with the galactocentric distance supporting the presence of a disc (see also Rampazzo et al. 2017). The disc is itself strongly perturbed by the interaction as can be deduced by the distortion in the NGC 454 T area (Fig. 1).

Both Johansson (1988) and Stiavelli et al. (1998) speculated whether the morphology of NGC 454 W pair member was a spiral or an irregular galaxy, before the interaction. The galaxy, strongly star-forming, dominates in the NUV images with respect to NGC 454 E. There is one piece of evidence coming out from our velocity map: no rotation pattern is revealed, even in the NGC 454 W1 complex. The velocity difference between the complexes reaches ≈ 140 km s $^{-1}$ (Fig. 4) if we include the NGC 454 SE and SW complexes, and it is about 60 km s $^{-1}$ considering only NGC 454 W1–W6. To summarize, if NGC 454 W was a former spiral galaxy, it appears completely distorted by the encounter and the latter is not at an early phase. In the next section, we will investigate the formation and evolution of this pair, highlighting a possible interaction that matches the global properties of this pair, i.e. its total magnitude, morphology and multi-wavelength spectral energy distribution (SED).

NGC 454 SW and SE have a projected separation of ≈ 37.19 (8.7 kpc) and ≈ 39.86 arcsec (9.4 kpc) from the centre of W1, i.e. they occupy a very peripheral position with respect to the bulk of the galaxy. Figs 1 and 2 both show that there is a very faint connection with the rest of the galaxy.

Our kinematical study suggests that the two complexes do not show a rotation pattern. So NGC 454 SW and SE differ from tidal dwarf candidates as described in Lelli et al. (2015). Fig. 6 shows that H α emission lines, detected also in between the SW and SE stellar complexes, are not composed of multiple components. According to the scheme proposed by Moiseev & Lozinskaya (2012), the

$(I-\sigma)$ plots (Fig. 7) suggest that the ionized gas in SW and SE stellar complexes has the characteristic of dense H II regions surrounded by low-density gas with considerable turbulent motions (see the scheme in their fig. 6) not dissimilar from the W2–W6 complexes.

To summarize, both the *Swift*-UVOT NUV observations and the diffuse H α emission indicate that NGC 454 W, NGC 454 SW and SE complexes are strongly star-forming regions. The anatomy of these complexes made using $(I-\sigma)$, $(I-V_r)$ and $(V_r-\sigma)$ diagnostic diagrams indicates that H II shells of different ages are present as well as zones of gas turbulence as expected by the interplay of star formation and supernova (SN) explosion in the Inter Galactic Medium. Although our observations did not reveal direct evidence of gas infall on the centre of NGC 454 E, there are signatures of recent star formation, in addition to the non-thermal type 2 Seyfert emission. Mendoza-Castrejón et al. (2015) reported the presence in *Spitzer*-InfraRed Spectrograph spectra of polycyclic aromatic hydrocarbons (PAHs) which are connected to recent star formation episodes (see e.g. Vega et al. 2010; Rampazzo et al. 2013, and references therein).

7.2 Possible evolutionary scenario

We investigate the evolution of the NGC 454 system using SPH simulation with chemo-photometric implementation (Mazzei, Marino & Rampazzo 2014, and references therein). Simulations have been carried out with different total mass (for each system from 10^{13} to $10^{10} M_{\odot}$), mass ratios (1:1–10:1), gas fraction (0.1–0.01) and particle number (initial total number from 40 000 to 220 000). All our simulations of galaxy formation and evolution start from collapsing triaxial systems (with triaxiality ratio, $\tau = 0.84$; Mazzei et al. 2014), composed of dark matter (DM) and gas and include self-gravity of gas, stars and DM, radiative cooling, hydrodynamical pressure, shock heating, viscosity, star formation, feedback from evolving stars and Type II SNe and chemical enrichment as in Mazzei & Curir (2003). We carried out different simulations varying the orbital initial conditions in order to have, for the ideal Keplerian orbit of two points of given masses, the first pericentre separation, p , equal to the initial length of the major axis of the more massive triaxial halo down to 1/10 of the same axis. For each pericentre separation, we changed the eccentricity in order to have hyperbolic orbits of different energy. The spins of the systems are generally

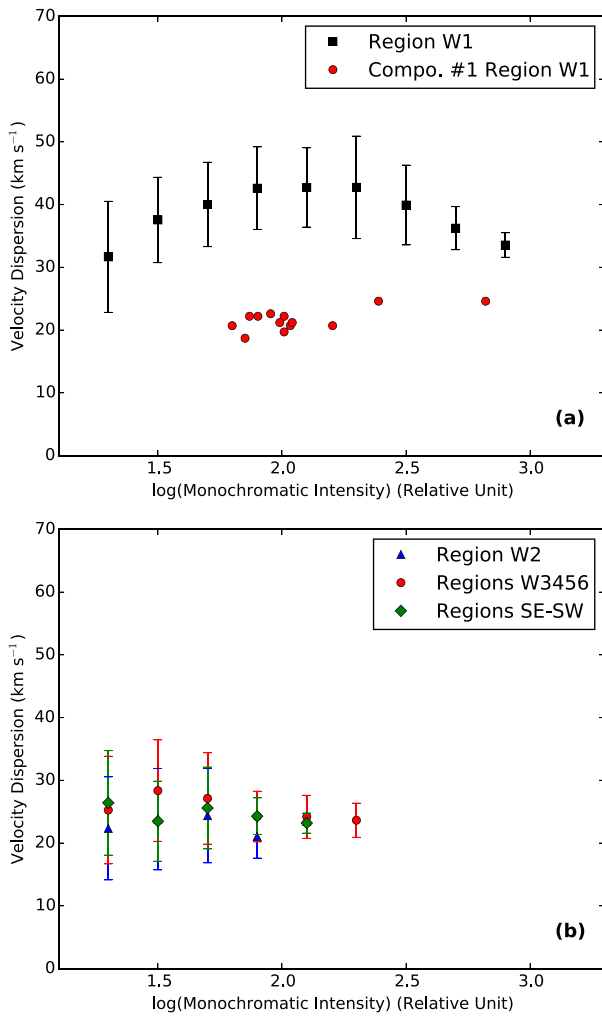


Figure 10. $(I-\sigma)$ diagnostic diagram for the W1 complex (top panel) and for the other complexes in NGC 454 W (bottom panel). The σ values are averaged over intensity bins. Red dots on the W1 complex show the main component in line profile decomposition shown in Fig. 9.

parallel to each other and perpendicular to the orbital plane, so we studied direct encounters. Some cases with misaligned spins have also been analysed in order to investigate the effects of the system initial rotation on the results. From our grid of simulations, we single out the one which simultaneously (i.e. at the same snapshot) accounts for the following observational constraints providing the best fit of the global properties of NGC 454: (i) total absolute B -band magnitude within the range allowed by observations (see below); (ii) the predicted SED in agreement with the observed one; (iii) morphology like the observed one in the same bands and with the same spatial scale (arcsec kpc^{-1}). The results we present are predictions of the simulation which best reproduces all the previous observational constraints at the same snapshot. This snapshot sets the age of the galaxy.

To obtain the SED of the whole system extended over the widest wavelength range, we add to our UV and optical *Swift*-UVOT total fluxes (green points in Fig. 11) the B , R and *IRAS* data (red points in Fig. 11) in NED, and the J , H , K total fluxes, derived from 2MASS archive images, which perfectly agree with J , H and K values reported by Tully (2015). All these data are corrected

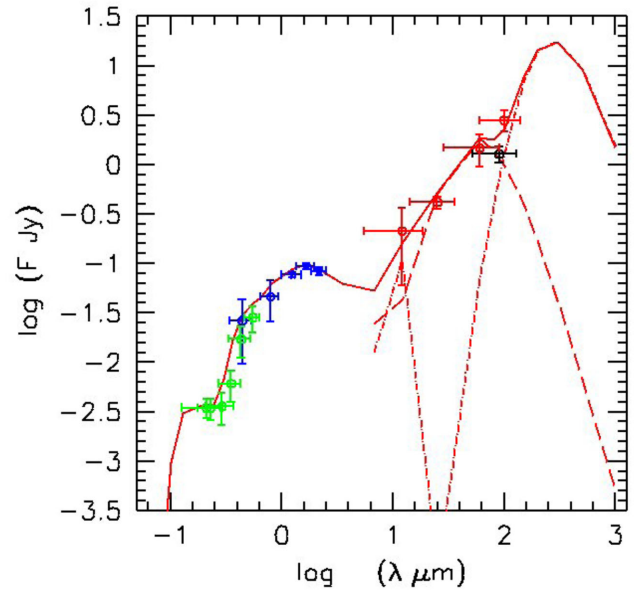


Figure 11. Observed SED of the whole NGC 454 system. The contribution of both the dust components to the FIR SED is also shown: dot-dashed and the long-dashed lines are the warm and the cold dust components, respectively (see the text). The solid line represents the resulting SED. Green symbols represent our *Swift*-UVOT observations and blue symbols B , R , *IRAS* and 2MASS J , H , K measures. Red symbols are *IRAS* data while the black symbol is the *AKARI*/FIS detection.

for galactic extinction as reported in Section 2.2 (Table 2) and Section 6. The black point in Fig. 11 is *AKARI*/Far Infrared Surveyor (FIS) detection. The solid line (red) in Fig. 11 highlights the predicted SED.

The simulation that provides this fit corresponds to a major merger between two haloes, initially of DM and gas, of equal mass and gas fraction (0.1), with perpendicular spins and total mass $4 \times 10^{12} M_{\odot}$. Their mass centres are initially 1.4 Mpc away from each other and move at a relative velocity of 120 km s^{-1} . Table 5 reports the input parameters of the SPH-Chemo-Photometric Implementation (CPI) simulation best fitting the global properties of the system. The age of the system is 12.4 Gyr at the best fit. The FIR SED accounts for a B -band attenuation of 0.85 mag so that the absolute B -band magnitude of the best-fitting snapshot is -21.0 mag. This is the value to be compared with that derived from the distance in Table 1 accounting for an error of ± 3.5 Mpc and a total B -band magnitude of 12.66 ± 0.21 mag (from Table 2), that is $M_B = -20.64 \pm 0.41$ mag.

Our fit of the FIR emission implies a warm dust component, heated by the UV radiation of H_{II} regions, and a cold component, heated by the general radiation field, both including PAH molecules as described in Mazzei, Xu & de Zotti (1992), Mazzei, de Zotti & Xu (1994) and Mazzei & Zotti (1994), with a relative contribution $r_{w/c} = 0.5$, which means that 30 per cent of the FIR emission is due to warm dust emission. The cutoff radius of the cold dust distribution in Fig. 11 is $100 r_c$, r_c being the core radius (Mazzei et al. 1994).

The shape of the FIR SED suggests the presence of a large amount of dust: the ratio between the FIR luminosity and the observed luminosity in the UV-to-near-IR (NIR) spectral range is 2.5.

Fig. 12 shows the morphology of our simulation at the best-fitting age to be compared with that in Fig. 2. We point out that the West component dominates the UV morphology and the East

Table 5. Input parameters of SPH-CPI simulation of NGC 454. Columns are as follows: (1) total number of initial ($t = 0$) particles; (2) length of the semi-major axis of the halo; (3) pericentric separation of the haloes in units of the semi-major axis; (4) and (5) distances of the halo centres of mass from the centre of mass of the total system, (6) and (7) velocity moduli of the halo centres in the same frame; (8) total mass of the simulation; (9) initial gas fraction of the haloes.

| N_{part} | a (kpc) | p/a | r_1 (kpc) | r_2 (kpc) | v_1 (km s^{-1}) | v_2 (km s^{-1}) | M_T ($10^{10} M_{\odot}$) | f_{gas} |
|-------------------|--------------|-------|----------------|----------------|---------------------------------|---------------------------------|----------------------------------|------------------|
| 60 000 | 1014 | 1/3 | 777 | 777 | 57 | 57 | 400 | 0.1 |

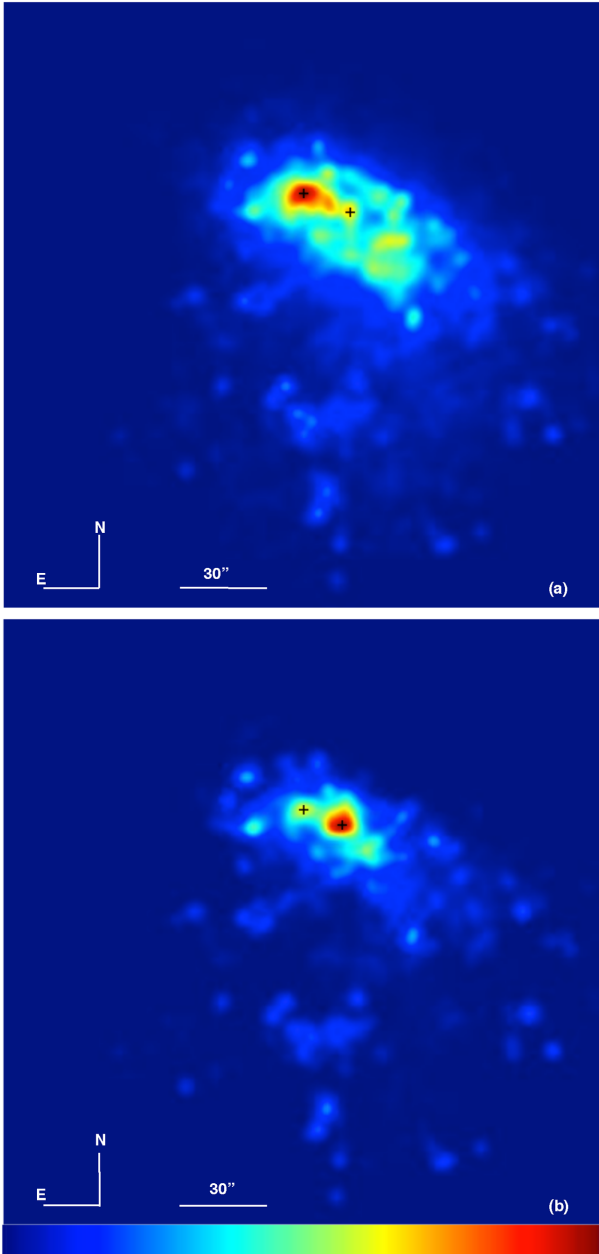


Figure 12. V-band (a) and UV [M2 band, (b)] xz projection of our simulation at the best-fitting age; maps are normalized to the total flux within the box, and account for dust attenuation with the same recipes used to provide the SED in Fig. 11. The scale is as in Fig. 2, with the density contrast being equal to 100. Crosses emphasize the nuclei of the merging galaxies, corresponding to E and Irr in Fig. 2, and N–E directions are given to guide the comparison.

component the optical one, as observed. The simulation shows that these systems will merge within 0.2 Gyr.

Therefore, our approach points towards a picture where E+S pairs can be understood in terms of 1:1 encounters, giving rise to a merger in less than 1 Gyr. Of course, this framework deserves further investigation, which is beyond the scope of this work.

8 SUMMARY AND CONCLUSIONS

We used SAM-FP observations at SOAR and *Swift*-UVOT archival images to investigate the kinematical and photometric properties of the NGC 454 interacting/merging system.

According to the definition in Stiavelli et al. (1998), we subdivided the system in NGC 454 E, the early-type member, NGC 454 T, the perturbed area to the North of NGC 454 W, the late-type member, and the two NGC 454 SW and SE complexes South of the late type. Further subdivision of the NGC 454 W member into W1–W6 has been used to detail single $H\alpha$ complexes revealed by the monochromatic map (see also Johansson 1988).

We found the following results.

(i) The $H\alpha$ map shows that the emission is mostly detected in the NGC 454 W system and in the NGC 454 SW and NGC 454 SE complexes. An $H\alpha$ broad emission is revealed in the centre of NGC 454 E, with a velocity gradient of 130 km s^{-1} across 4 arcsec.

(ii) The radial velocity map does not have a rotation pattern neither in the W1–W6 complexes in NGC 454 W nor in the two SW and SE complexes. W6 shows a velocity gradient of 45 km s^{-1} .

(iii) The velocity dispersion map shows that most of the W3–W6, SW and SE complexes have a velocity dispersion in the range $20\text{--}25 \text{ km s}^{-1}$. The highest velocity dispersion, 68 km s^{-1} , and the lowest, 15 km s^{-1} , are measured in the W1 and W2 complexes, respectively.

We use $(I-\sigma)$, $(I-V)$ and $(\sigma-V)$ (see e.g. Bordalo et al. 2009) diagnostic diagrams to study the kinematics of the W1–W6 complexes in NGC 454 W and the SW and SE complexes. Diagnostic diagrams show that all regions, except W1 and SW1, have a weak-to-moderate correlation between the radial velocity and the dispersion interpreted as systematic motions towards or away from the observer. These diagrams confirm that W1 has a high supersonic velocity dispersion and a closer analysis could separate two populations, one in the centre with a low dispersion and a second around it with a higher σ . According to Moiseev & Lozinskaya (2012), W1 could show a GH nR in the centre and a turbulent low-density gas cloud in its outskirts. This picture can be discussed further if we take into account the several large profiles in W1 that show multiple components. If we only take into account the main component (the brightest), the situation is reversed, with a broader line in the centre and narrowed ones around. This can be interpreted as an expanding wind-blown bubble according to Lagrois & Joncas (2009).

Based on our SPH simulation with chemo-photometric implementation, the global properties of the system, 12.4 Gyr old, are compatible with an encounter between two haloes of equal mass and perpendicular spin. They will merge within 0.2 Gyr. The SED suggests a large FIR emission 2.5 times that in the NUV–NIR range.

The case of NGC 454 system suggests that a class of mixed pairs form via the encounter/merging of similar-mass, evolving haloes. The different morphologies, emphasized by multi- λ observations, mark a late phase of the merging process.

ACKNOWLEDGEMENTS

This work is based on observations obtained at the Southern Astrophysical Research (SOAR) telescope, which is a joint project of the Ministério da Ciência, Tecnologia, e Inovação (MCTI) da República Federativa do Brasil, the US National Optical Astronomy Observatory (NOAO), the University of North Carolina at Chapel Hill (UNC) and Michigan State University (MSU). We would like to warmly thank A. Tokovinin, C. Mendes de Oliveira and B. Quint for their participation during the run and without which the commissioning of the instrument and the run would not have been possible. We would also like to thank the anonymous referee for his useful corrections. HP thanks SOAR staff. He also thanks Aix Marseille Université for its financial support during his visit at Laboratoire d’Astrophysique de Marseille in 2017 April–July. PM and RR acknowledge support from INAF through grants PRIN-2014-14 ‘Star formation and evolution in galactic nuclei’ and PRIN-SKA 2016 ‘Empowering SKA as a probe of galaxy evolution with H I’. We acknowledge the usage of the HyperLeda data base (<http://leda.univ-lyon1.fr>). Part of this work is based on archival data, software or online services provided by the ASI Science Data Center. This research has made use of the NASA/IPAC Extragalactic Database (NED) which is operated by the Jet Propulsion Laboratory, California Institute of Technology, under contract with the National Aeronautics and Space Administration.

REFERENCES

- Amram P., Balkowski C., Boulesteix J., Cayatte V., Marcellin M., Sullivan W. T., III, 1996, *A&A*, 310, 737
- Arp H. C., Madore B. F., 1987, *A Catalogue of Southern Peculiar Galaxies and Associations*. Cambridge Univ. Press, Cambridge
- Barton E. J., 2000, PhD thesis, Harvard University, Cambridge
- Barton Gillespie E., Geller M. J., Kenyon S. J., 2003, *ApJ*, 582, 668
- Benaglia T., Chauveau D., Hunter D. R., Young R. S., 2009, *J. Stat. Softw.*, 32, 1
- Bordalo V., Plana H., Telles E., 2009, *ApJ*, 696, 1668
- Breeveld A. A. et al., 2010, *MNRAS*, 406, 1687
- Breeveld A. A., Landsman W., Holland S. T., Roming P., Kuin N. P. M., Page M. J., 2011, in McEnery J. E., Racusin J. L., Gehrels N., eds, *AIP Conf. Proc. Vol. 1358, Gamma Ray Bursts 2010*. Am. Inst. Phys., New York, p. 373
- Combes F., Prugniel P., Rampazzo R., Sulentic J. W., 1994, *A&A*, 281, 725
- de Mello D. F., Sulentic J. W., Rampazzo R., 1995, *Astrophys. Lett. Commun.*, 31, 325
- de Mello D. F., Sulentic J. W., de Souza R. E., Reduzzi L., Rampazzo R., 1996, *A&A*, 308, 387
- de Vaucouleurs G., 1948, *Ann. Astrophys.*, 11, 247
- Domingue D. L., Sulentic J. W., Xu C., Mazzarella J., Gao Y., Rampazzo R., 2003, *AJ*, 125, 555
- Donzelli C. J., Pastoriza M. G., 2000, *AJ*, 120, 189
- Einasto M. et al., 2010, *A&A*, 522, A92
- Elmegreen B. G., Kaufman M., Thomasson M., 1993, *ApJ*, 412, 90
- Elmegreen D. M., Kaufman M., Brinks E., Elmegreen B. G., Sundin M., 1995, *ApJ*, 453, 100
- Epinat B. et al., 2008, *MNRAS*, 388, 500
- Faber S. M. et al., 2007, *ApJ*, 665, 265
- Font J. et al., 2011, *ApJ*, 740, L1
- Fraga L., Kunder A., Tokovinin A., 2013, *AJ*, 145, 165
- Fraley C., Raftery A. E., 2007, *J. Stat. Softw.*, 18, 1
- Freeman K. C., 1970, *ApJ*, 160, 811
- Horellou C., Booth R., 1997, *A&AS*, 126, 3
- Ihaka R., Gentleman R., 1996, *J. Comput. Graph. Stat.*, 5, 299
- Irwin J. A., 1994, *ApJ*, 429, 618
- Jedrzejewski R., 1987, *MNRAS*, 226, 747
- Johansson L., 1988, *A&A*, 191, 29
- Karachentsev I. D., 1972, *Comm. Spec. Astrophys. Obs. USSR*, 7, 1
- Karczewski O. L. et al., 2013, *MNRAS*, 431, 2493
- Knapen J., Querejeta M., 2015, *Galaxies*, 3, 220
- Lagrois D., Joncas G., 2009, *ApJ*, 691, 1109
- Larson R. B., Tinsley B. M., 1978, *ApJ*, 219, 46
- Laval A., Boulesteix J., Georgelin Y. P., Georgelin Y. M., Marcellin M., 1987, *A&A*, 175, 199
- Lelli F., Duc P.-A., Brinks E., McGaugh S., 2015, *Galaxies*, 3, 184
- Lin L. et al., 2008, *ApJ*, 681, 232
- Marchese E., Braitto V., Della Ceca R., Caccianiga A., Severgnini P., 2012, *MNRAS*, 421, 1803
- Marino A. et al., 2011, *MNRAS*, 411, 311
- Marino A., Mazzei P., Rampazzo R., Bianchi L., 2016, *MNRAS*, 459, 2212
- Markwardt C. B., 2009, in Bohlender D. A., Durand D., Dowler P., eds, *ASP Conf. Ser. Vol. 411, Astronomical Data Analysis Software and Systems XVIII*. Astron. Soc. Pac., San Francisco, p. 251
- Mazzei P., Curir A., 2003, *ApJ*, 591, 784
- Mazzei P., de Zotti G., 1994, *MNRAS*, 266, 5
- Mazzei P., Xu C., de Zotti G., 1992, *A&A*, 256, 45
- Mazzei P., de Zotti G., Xu C., 1994, *ApJ*, 422, 81
- Mazzei P., Marino A., Rampazzo R., 2014, *ApJ*, 782, 53
- Mendes de Oliveira C., Amram P., Quint B., Torres-Flores S., Barbá R., Andrade D., 2017, *MNRAS*, 469, 3424
- Mendoza-Castrejón S., Dultzin D., Krongold Y., González J. J., Elitzur M., 2015, *MNRAS*, 447, 2437
- Moiseev A. V., Lozinskaya T. A., 2012, *MNRAS*, 423, 1831
- Morrissey P. et al., 2007, *ApJS*, 173, 682
- Muñoz-Tuñón C., Tenorio-Tagle G., Castañeda H. O., 1996, *AJ*, 112, 1636
- Oke J. B., 1974, *ApJS*, 27, 21
- Peterson S. D., 1979, *ApJS*, 40, 527
- Poole T. S. et al., 2008, *MNRAS*, 383, 627
- Prugniel Ph., Héraudeau Ph., 1998, *ApJS*, 128, 299
- Rampazzo R., Sulentic J. W., 1992, *A&A*, 259, 43
- Rampazzo R., Reduzzi L., Sulentic J. W., Madejsky R., 1995, *A&AS*, 110, 131
- Rampazzo R. et al., 2006, *MNRAS*, 368, 851
- Rampazzo R. et al., 2007, *MNRAS*, 381, 245
- Rampazzo R. et al., 2011, *Ap&SS*, 335, 201
- Rampazzo R., Panuzzo P., Vega O., Marino A., Bressan A., Clemens M. S., 2013, *MNRAS*, 432, 374
- Rampazzo R. et al., 2016, in *Astrophysics and Space Science Library*, Vol. 435, *From the Realm of the Nebulae to Populations of Galaxies*. Springer, Berlin, p. 381
- Rampazzo R., Mazzei P., Marino A., Uslenghi M., Trinchieri G., Wolter A., 2017, *A&A*, 602, A97
- Reduzzi L., Rampazzo R., 1995, *Astrophys. Lett. Commun.*, 30, 1 (RR23)
- Roming P. W. A. et al., 2005, *Space Sci. Rev.*, 120, 95
- Ruckdeschel P., Kohl M., Stabla T., Camphausen F., 2006, *R News*, 6, 2
- Sérsic J. L. ed., 1968, *Atlas de Galaxias Australes*. Observatorio Astronómico, Córdoba, Argentina
- Shuder J. M., Osterbrock D. E., 1981, *ApJ*, 250, 55
- Smith M., Weedman D., 1970, *ApJ*, 161, 33

- Smith B. J., Struck C., Hancock M., Appleton P. N., Charmandaris V., Reach W. T., 2007, *AJ*, 133, 791
- Smith B. J., Zaragoza-Cardiel J., Struck C., Olmsted S., Jones K., 2016, *AJ*, 151, 63
- Soares D. S. L., de Souza R. E., de Carvalho R. R., Couto da Silva T. C., 1995, *A&AS*, 110, 371
- Stiavelli M., Panagia N., Carollo M. C., Romaniello M., Heyer I., Gonzaga S., 1998, *ApJ*, 492, L135
- Struck C., 2011, *Galaxy Collisions*. Springer, New York
- Surace J. A., Mazzarella J., Soifer B. T., Wehrle A. E., 1993, *AJ*, 105, 864
- Tanvuia L., Kelm B., Focardi P., Rampazzo R., Zeilinger W. W., 2003, *AJ*, 126, 1245
- Tokovinin A., Cantarutti R., Tighe R., Schurter P., van der Bliik N., Martinez M., Mondaca E., 2010a, *PASP*, 122, 1483
- Tokovinin A. et al., 2010b, *Proc. SPIE*, 7736, 77363L
- Tully B. R., 2015, *AJ*, 149, 117
- van Dokkum P. G., 2001, *PASP*, 113, 1420
- van Dokkum P. G., 2005, *ApJ*, 130, 2647
- Vega O. et al., 2010, *ApJ*, 721, 1090
- Xu C., Sulentic J. W., 1991, *ApJ*, 373, 407
- Zaragoza-Cardiel J. et al., 2013, *MNRAS*, 432, 998
- Zaragoza-Cardiel J. et al., 2015, *MNRAS*, 451, 1307

APPENDIX A: THE ENVIRONMENT OF THE NGC 454 SYSTEM

The NGC 454 system is an isolated pair, RR23, in the Reduzzi & Rampazzo (1995) catalogue. Assuming the distance given in Table 1, we used HyperLeda to inspect a box of 4×4 Mpc² for possible neighbours of this nearby system. Table A1, which includes the pair members, provides the galaxy identification (columns 1 and 2), the right ascension and declination (columns 3 and 4), the morphological type (column 5), the heliocentric velocity (column 6), the major axis diameter d_{25} (column 7), the axial ratio r_{25} (column 8) at $\mu_B = 25$ mag arcsec⁻², the position angle (column 9) and the total B -band apparent magnitude (column 10).

Most of the galaxies in Table A1 are listed in *A Catalogue of Southern Peculiar Galaxies and Associations* (Arp & Madore 1987) where they are recognized either to show peculiar features (AM 0058-580: compact galaxy with diametric jets; AM 0102-573: disrupted galaxy + two companions; AM 0126-525: ring or galaxy with loop; AM 0126-515: disturbed spiral) or to be pair members (like our NGC 454 system, i.e. AM 112-554: I/A double + resolved knots).

Fig. A1 shows the histogram of the recession velocity distribution (1000–6000 km s⁻¹) in an area of 4×4 Mpc² around NGC

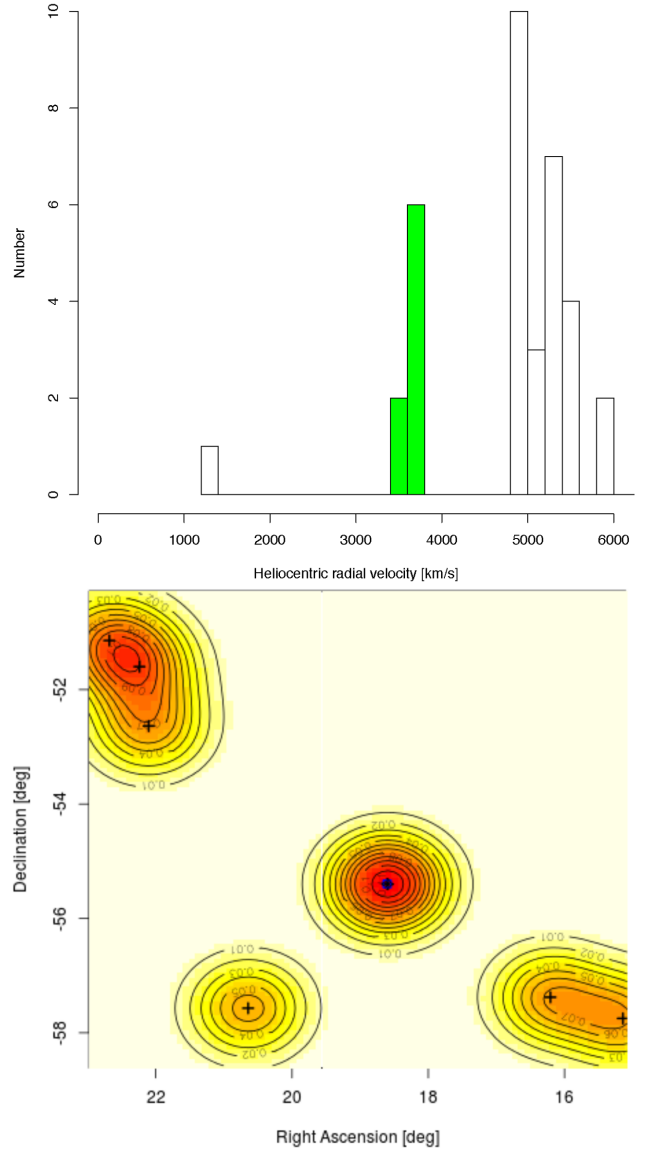


Figure A1. Top panel: histogram of the heliocentric radial velocity of galaxies within a box of 4×4 Mpc² in the range 1000–6000 km s⁻¹. Bottom panel: spatial distribution of galaxies in green in the top panel, i.e. the neighbours of the NGC 454 system. The map is normalized to the total density. Galaxies in the area are listed in Table A1.

Table A1. Galaxies in 4×4 Mpc² around the NGC 454 system. For each galaxy, the columns provide the following information: (1) the galaxy identification, (2,3) the (J2000) galaxy coordinates, (4) the morphological type, (5) the heliocentric velocity, (6) the log of the length of the projected major axis of a galaxy at the isophotal level of 25 mag arcsec⁻² in the B band, (7) the log of the axial ratio (major axis/minor axis) of the isophote at 25 mag arcsec⁻² in the B band, (8) the position angle and (9) the total apparent B -band magnitude. Data are from Hypercat. Other identification is from NED.

| Ident. | Other Ident. F | RA (2000) (deg) | Dec. (2000) (deg) | T | V_h (km s ⁻¹) | $\log d_{25}$ $\log[0.1 \text{ arcmin}]$ | $\log r_{25}$ | PA (deg) | B_T (mag) |
|------------|---------------------|--------------------|----------------------|------|--------------------------------|---|---------------|-------------|------------------|
| ESO113-004 | AM 0058–580 | 1.009 50 | –57.748 30 | 5.0 | 3566 ± 67 | 0.75 | 0.19 | 105.5 | 15.04 ± 0.20 |
| ESO113-009 | AM 0102-573 | 1.080 46 | –57.377 42 | 10.0 | 3648 ± 6 | 0.99 | 0.54 | 165.4 | 16.02 ± 0.20 |
| NGC 454 W | RR023a | 1.239 45 | –55.400 13 | –1.0 | 3626 ± 2 | 1.22 | 0.00 | – | 13.12 ± 0.20 |
| NGC 454 E | AM 0112-554; RR023b | 1.240 25 | –55.397 14 | –2.0 | 3635 ± 2 | 1.28 | 0.38 | 80.9 | 13.14 ± 0.20 |
| ESO113-044 | – | 1.376 32 | –57.569 19 | 10.0 | 3616 ± 8 | 0.67 | 0.15 | 53.3 | 16.99 ± 0.20 |
| PGC005497 | AM 0126-525 | 1.473 67 | –52.635 88 | 9.0 | 3450 ± 42 | 0.92 | 0.34 | 92.7 | 16.78 ± 0.20 |
| NGC0576 | AM 0126-515 | 1.482 69 | –51.598 71 | –1.1 | 3604 ± 39 | 0.99 | 0.08 | – | 14.42 ± 0.19 |
| ESO196-011 | – | 1.512 17 | –51.141 89 | 5.8 | 3634 ± 6 | 1.25 | 0.42 | 12.6 | 14.47 ± 0.20 |

454 and the spatial distribution in the same area of the nearby galaxies, shown in green in the top panel. The nearby neighbours are disc galaxies either S0s or spirals according to the classification of HyperLeda. The velocity dispersion of these galaxies is 65 km s^{-1} . This value has to be compared with $327_{-2}^{+12} \text{ km s}^{-1}$ of NGC 5486, the third rich galaxy association in the nearby Universe (Marino et al. 2016), and with $92_{-2}^{+3} \text{ km s}^{-1}$ of LGG 225, a very

loose group discussed in Mazzei et al. (2014). This picture confirms that the NGC 454 system is isolated and located in a very poor environment (see also Tully 2015).

This paper has been typeset from a \TeX/L\TeX file prepared by the author.